Journal of Atmospheric and Solar–Terrestrial Physics 247 (2023) 106074

Contents lists available at ScienceDirect

Journal of Atmospheric and Solar-Terrestrial Physics

journal homepage: www.elsevier.com/locate/jastp

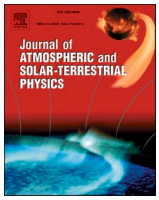

Research Paper

Lower-ionosphere electron density and effective recombination coefficients from multi-instrument space observations and ground VLF measurements during solar flares

Vida Žigman [a,*], Marie Dominique [b], Davorka Grubor [c], Craig J. Rodger [d], Mark A. Clilverd [e]

[a] University of Nova Gorica, Vipavska cesta 13, 5000, Nova Gorica, Slovenia
[b] Royal Observatory of Belgium, 3 Avenue Circulaire, B-1180, Brussels, Belgium
[c] University of Belgrade, Faculty of Mining and Geology, Physics Cathedra, Djusina 7, 11000, Belgrade, Serbia
[d] Department of Physics, University of Otago, PO Box 56, Dunedin, 9054, New Zealand
[e] British Antarctic Survey (UKRI-NERC), High Cross, Madingley Road, Cambridge, CB3 0ET, UK

ARTICLE INFO

Handling Editor: Dora Pancheva

Keywords:
Solar flares
Solar spectral irradiance
Ionosphere
VLF
Time delay
Electron density

ABSTRACT

A new model to predict the electron density and effective recombination coefficient of the lower ionosphere under solar flare conditions is presented. This model relies on space-borne solar irradiance measurements in coincidence with ground recorded active transmissions of Very Low Frequency (VLF), (<30 kHz) signals. Use is made of the irradiance measured by broad-band radiometers onboard the satellites: GOES, SDO, and PROBA2. Measurements are made over succeeding and partly overlapping wavelength intervals of the instrument bandpass ranges altogether covering the range 0.1–20 nm. The aim is to determine the effectiveness of the particular instrument bandpass in producing changes in the ionization of the lower ionosphere (D-region) during solar X-ray flares. Ionization efficiency is evaluated using modelled Solar Spectral Irradiance for each flare separately and for each instrument as a function of its bandpass.

The new model is based on coupling of the continuity equation with the Appleton relation and uses the concept of time delay – the time lag of the extreme VLF amplitude and phase behind the flare irradiance maximum. The solution of the continuity equation predicts the electron density time - height profile for 55–100 km altitude.

An analysis of M to X class flares shows the flare-enhanced electron densities due to a particular ionizing wavelength domain are in good agreement for the case where irradiance is taken over the bandpass of (1) either GOES (0.1–0.8 nm) or SDO/ESP (0.1–7 nm) for up to 90 km (2) either SDO/ESP or PROBA2/LYRA (1–2 +6–20 nm) at heights above 90 km. The results agree within 22% for heights up to 90 km, and differ by at most a factor of 2 for heights above 90 km. Remarkable agreement is shown between measured and evaluated time delay; discrepancies are generally less than 8%. The effective recombination coefficient is deduced from the model itself and is found to be consistent with other independent estimates.

1. Introduction

Studies of solar flares based on satellite recordings of solar irradiance, traditionally in the soft X-ray band (0.1–0.8 nm), coupled to coincident ground-based subionospheric propagation-detected changes in Very Low Frequency (VLF) waves (<30 kHz) is a well-established research approach. This has allowed continuous improvements in our understanding of the flare disturbed lower ionosphere, particularly in the D-region (e.g. Mitra, 1974; Hayes et al., 2017; George et al., 2019; Belcher et al., 2021). Data used in relevant studies have been gathered from recordings on various VLF paths all over the globe, and have been studied in correlation with X-ray fluxes. Core papers that have paved the way for further VLF research include, for example, Thomson, 1993; Thomson and Clilverd, 2000, 2001; McRae and Thomson, 2000, 2004; Thomson et al., 2004, 2005, 2011, 2017.

The present revival of these studies rests, to a large extent, on the constantly increasing availability of refined space sensors operating on different portions of the X-ray and EUV spectra and the consolidation of

* Corresponding author.
E-mail address: vida.zigman@ung.si (V. Žigman).

https://doi.org/10.1016/j.jastp.2023.106074
Received 30 May 2022; Received in revised form 13 April 2023; Accepted 16 April 2023
Available online 22 April 2023

networks of VLF receivers worldwide (e.g. Clilverd et al., 2009; Wenzel et al., 2016). There are current developments in the modelling of satellite measurements of solar irradiance, resulting in upgraded Solar Spectral Irradiance (SSI) models, (e.g. Woods et al., 2008, 2012; Chamberlin et al., 2008, 2020). Ongoing advances in VLF propagation include VLF modal theory (Cummer, 2000; Gross et al., 2018), flare spectral analysis associated with VLF detection (Briand et al., 2022), and improved description of D-region production-loss processes (Thomson et al., 2022).

The present work both builds on, and adds to these studies with regard to observations and modelling, with the goal being to increase the understanding of the solar flare phenomena and, in particular, flare impact on the lower ionosphere. Parallel observations of Integrated Solar Irradiance (ISI) time series in the Soft X-Ray (X-ray or XUV) and EUV range (up to 20 nm) by instruments on board of the Geostationary Operational Environment Satellites (GOES), the Solar Dynamic Observatory (SDO) and the Project for On-Board Autonomy-2 (PROBA-2) missions, are used to study representative flare events throughout their duration. We use these observations to evaluate how the flare enhancement in different spectral bands affects the ionospheric response at different altitudes of the lower ionosphere. We examine heights that encompass the ionospheric D-region, and its upper boundary, by considering an altitude range of 55–100 km.

Irradiance measurements are related to ground-based measurements of active transmissions of VLF radio waves, which readily sense the ionization changes in the lower ionosphere. Inspection of flare enhanced ISI in conjunction with observations of disturbed VLF subionospheric changes of amplitude and phase (A,P), lead to the identification of a *time delay* (Appleton, 1953) correlating the two datasets. However, in VLF propagation studies, it is common in the literature that the primary focus is given to amplitude observations (e.g. Hayes et al., 2021; Briand et al., 2022). This limitation is addressed in the work described here.

In the present study, an improved physics-based model, $N(t, h)$, relying on the continuity equation, an extension of the $N(t)$ model (Žigman et al., 2007), is advanced to quantify the flare-induced enhancement of D-region electron density *time-height* profile. The height-dependent integral ionization efficiency corresponding to several instrument wavelength bands is calculated on the basis of modelled SSI (Woods et al., 2008, 2012), for each of the representative M- and X-class flares, mainly from the beginning of Solar Cycle 24. The electron density $N(t,h)$ results compare favourably with predictions of the standard model of VLF propagation (Long Wavelength Propagation Code (LWPC) (Ferguson, 1998), which infers electron density height profiles by simulating measured $(A,\ P)$ changes.

In a further improvement, measurements of *both* VLF parameters $(A,\ P)$ are considered on equal terms, which is necessary to accomplish accurate and reliable ionospheric modelling (Gross et al., 2018; Thomson et al., 2022). Consequently, along with the amplitude time delay (e.g. Žigman et al., 2007; Hayes et al., 2021), the *phase time delay* is here first presented and used in calculations. The evaluated electron density time profiles provide amplitude and phase time delays in notable agreement with measured ones.

One important property of the $N(t,h)$ model is that the effective recombination coefficient is determined within the model itself, thus comparison with other independent observations and models is meaningful. The evaluated effective recombination coefficient compares favourably with the values obtained by rocket-based measurements (Friedrich et al., 2004) and those presented by Osepian et al. (2009) for disturbed ionospheric conditions. For an outstanding space weather event, electron density time-height profiles evaluated with the $N(t,h)$ model are found to be in remarkable agreement with radar measurements (Häggström, 2005; Singer et al., 2011).

Thus in this study an improved physics-based model is presented which accurately reproduces observed time delays for solar flare responses in the ionospheric D-region, and also calculates realistic D-region electron density time-height profiles during flare events.

The rest of the paper is organized as follows: Section 2 describes the experimental data and details the flare selection criteria. Section 3 refers to the modelling procedures of the basic input datasets for the solving of the continuity equation. The new $N(t,h)$ model is presented in Section 4 along with the short overview of the benchmark LWPC code. Section 5 presents the results arrived at in the present study and provides comparison with other independent findings. Section 6 accounts for the efficiency of different bandpass ranges in ionizing the lower ionosphere, and discusses the importance of amplitude and phase time delay. Section 7 provides concluding remarks.

2. Observations

Space-borne irradiance and ground-based VLF observations were used to determine the electron density enhancement during solar flares.

Irradiance observations refer to broadband measurements of the full-Sun Integrated Solar Irradiance (ISI) I [Wm^{-2}] by radiometers onboard the GOES, SDO and PROBA2 satellites, over their respective bandpass ranges:

1) I_{GOES} refers to observations by the **GOES** X ray Sensor (XRS), with its 0.1–0.8 nm channel https://www.ngdc.noaa.gov/stp/satellite/goes/dataaccess.html. Scale factors are removed from the XRS distributed values (division by a factor 0.7), following the advice in Machol et al., 2022, to get the true physical irradiance values. Such corrected fluxes and corresponding flare indices will agree with those of the GOES-R series. The corrected flare classification is used throughout this work.
2) I_{ESP} refers to observations by the SDO/Extreme ultraviolet Variability Experiment (EVE), **E**UV **S**pectro**P**hotometer-Q (**ESP**), channel covering the 0.1–7 nm bandpass (Woods et al., 2012, https://lasp.colorado.edu/home/eve/).
3) I_{LYRA} refers to observations by the PROBA-2/**L**arge **Y**ield **RA**diometer, (**LYRA**), with the Zirconium channel of its nominal unit, covering the 1–2 + 6–20 nm bandpass (Dominique et al., 2013, https://proba2.sidc.be).

VLF measurements refer to narrowband radio broadcast signals of well stabilized frequency, (A,P) emitted from ground-based VLF transmitters (Tx), namely: GVT/22.1 kHz, NAA/24.0 kHz, NPM/21.4 kHz, and NWC/19.8 kHz, as identified by their call sign/carrier frequency. The respective signal (A,P) measurements are taken at two ground-based receiver sites (Rx): Belgrade, Serbia (44.85° N, 20.38° E) and Casey, Antarctica (66.28° S, 110.53° E), which are both capable of monitoring multiple narrowband transmissions. The geographical coordinates of the selected Txs and Rxs, with the respective Great Circle Paths, ('path' for short), are shown in Fig. 1. It can be appreciated from Fig. 1, that d*ifferent* transmission and receiving sites were selected so as to provide both short (few Mm) and long (about a dozen Mm) paths, including transequatorial ones.

The Belgrade VLF observatory runs the Absolute Phase and Amplitude Logger (AbsPAL) receiving system with an aerial electric field antenna and the Casey VLF station in Antarctica operates the UltraMSK receiver with the vertical magnetic loop antenna. The two facilities measure amplitudes in units of dB above 1 μV/m and phase in degrees (Žigman et al., 2007; Clilverd et al., 2009). The locations of the two receiving sites, (roughly 14.5 Mm apart), provide complementing coverage of sunlit Tx to Rx paths over the 24-h day.

All timeseries were rebinned to a 1-min time resolution.

2.1. Correlation of measurements: solar X-ray (XUV) and EUV flare irradiance versus VLF ground measurements

Ionospheric disturbances caused by sudden X-ray bursts from solar flares are most distinctly imprinted on the VLF signal. The amplitude

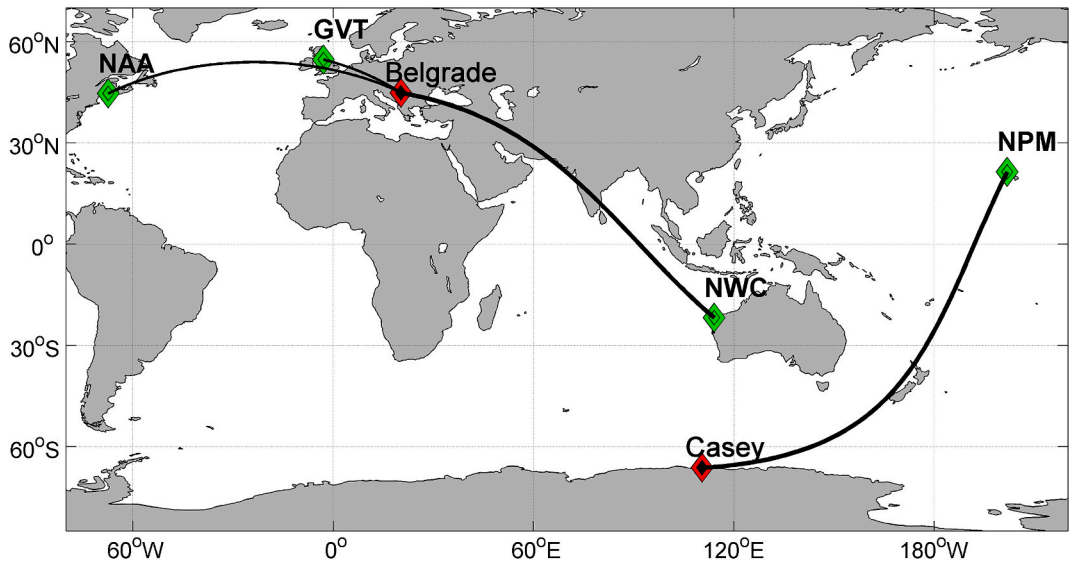

Fig. 1. Subionospheric VLF great circle paths between the transmitters (Tx) and receiving VLF stations (Rx) used in this study (black lines) shown in geographic coordinates. Green rhombs indicate the transmitter locations and the red ones the VLF station locations. (For interpretation of the references to colour in this figure legend, the reader is referred to the Web version of this article.)

and phase either abruptly increases or decreases, followed by a subsequent recovery. This signature unambiguously corresponds to flare occurrence, remarkably mimicking the flare irradiance rise and decay as measured by space-borne instruments. Our detailed parallel inspection of I_{GOES} and (A, P) data, within the duration of the flare (mostly from 20 min to hours), reveals a characteristic feature – almost regular (in 90% of analyzed events) – the extreme amplitude and/or phase peak is *delayed* in time with respect to the flare irradiance maximum. However, for strong flares, X3 and above, it is noticed that amplitude/phase, or both may reach the respective extremum *before* the irradiance peak.

The time interval by which the *extreme* amplitude and/or phase lags behind the flare maximum is the *time delay* Δt, more precisely, *both* amplitude and phase time delays, Δt_A and Δt_P respectively, can be identified. With the chosen time resolution, the presently observed Δt_A and Δt_P usually amount from 1 to several minutes. Though of the same order of magnitude, either $\Delta t_A \leq \Delta t_P$ or $\Delta t_A > \Delta t_P$ can occur for a particular flare, depending on the flare class and on the VLF Tx to Rx path. In the current study we consider Δt_P, which to the best knowledge of the authors has not previously been reported in the literature. The values of Δt_A found in our study are consistent with those from previous findings (Žigman et al., 2007) and the reported observations of other authors (e.g. Milligan et al., 2020; Hayes et al., 2021).

We present a study of flares as detected in parallel by GOES, ESP and LYRA and by the VLF propagation by focusing on the following flare events, designated by their flare class and peak time as registered by GOES, i.e. in chronological order: the M9.4 flare on 2011-02-18 10:11 UT, the M1.4 flare on 2011-02-18 14:08 UT, and the X1.9 flare on 2012-03-07 01:15 UT. We find it worthwhile to also include the X5.5 flare on

Table 1
Flare event parameters from ground VLF and space GOES, ESP and LYRA observations.

FLARE CLASS yyyy-mm-dd hh:mm UT	Instr.	$t(I_{\max})$ **UT**	$I_{\max}$ [Wm^{-2}]	$(\Delta t_A, \Delta t_P)$ [min]	
				NWC-Bel	GVT-Bel
M9.4	GOES15	10:11	9.44057 10^{-5}	(2,3)	(2,2)
2011-02-18 10:11	ESP	10:12	0.0085	(1,2)	(1,1)
	LYRA	10:12	0.00335	(1,2)	(1,1)
VLF path: NWC-Bel		$t(A_{\max}, P_{\max})$ UT (10:13, 10:14)	Great Circle Path distance = 11974 km; [Tx:NWC/19.8 kHz, North West Cape, Exmouth, Australia (21.82° S, 114.18° E); Rx: Belgrade (44.85° N, 20.38° E)]		
VLF path: GVT-Bel		$t(A_{\max}, P_{\min})$ UT (10:13, 10:13)	Great Circle Path distance = 2000 km; [Tx: GVT/22.1 kHz, Skelton, UK (54.72° N, 2.88° W); Rx: Belgrade (44.85° N, 20.38° E)]		
FLARE	Instr.	$t(I_{max})$ UT	$I_{\max}$ [Wm^{-2}]	$(\Delta t_A, \Delta t_P)$ [min] GVT-Bel	
M1.4	GOES15	14:08	1.43786 10^{-5}	(3, 1)	
2011-02-18 14:08	ESP	14:09	0.0022707	(2, 0)	
	LYRA	14:09	0.001612	(2, 0)	
VLF path: GVT-Bel		$t(A_{\min}, P_{\max})$ UT (14:11, 14:09)	Great Circle Path distance = 2000 km; [Tx: GVT/22.1 kHz, Skelton, UK (54.72° N, 2.88° W); Rx: Belgrade (44.85° N, 20.38° E)]		
FLARE	Instr.	$t(I_{\max})$ UT	$I_{\max}$ [Wm^{-2}]	$(\Delta t_A, \Delta t_P)$ [min] NPM-Casey	
X1.9	GOES15	01:15	1.95714 10^{-4}	(2.5, 3.5)	
2012-03-07 01:15	ESP	01:15	0.02107	(2.5, 3.5)	
	LYRA	01:15	0.00869	(2.5, 3.5)	
VLF path: NPM-Casey		$t(A_{\max}, P_{\max})$ UT (01:17.5, 01:18.5)	Great Circle Path distance = 12229 km; [Tx: NPM/21.4 kHz, Lualualei, Hawaii, USA (21.42° N, 158.15° W); Rx: Casey, Antarctica (66.28° S, 110.53° E)]		

Table 2
Flare event parameters from ground VLF and space GOES observations.

FLARE CLASS yyyy-mm-dd hh:mm UT	Instr.	$t(I_{max})$ UT	I_{max} [Wm^{-2}]	Δt_P [min]
				NAA-Bel
X5.9 2005-01-17 09:52	GOES10	09:52.5	5.94286 10^{-4}	0.5
X5.5 2005-01-17 09:52	GOES12	09:52	5.51429 10^{-4}	1
VLF path: NAA-Bel		$t(P_{max})$ UT 09:53	Great Circle Path distance = 6560 km; [Tx: NAA/24.0 kHz, Cutler, Maine, USA (44.63° N, 67.28° W); Rx: Belgrade (44.85° N, 20.38° E)]	

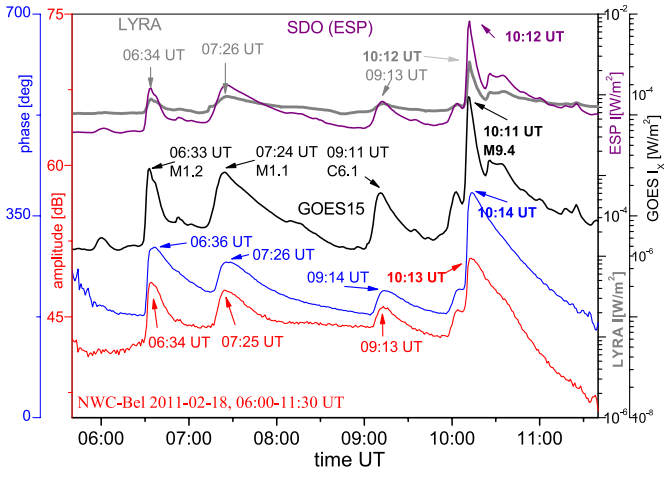

Fig. 2. Integrated Solar Irradiance (ISI) on the active day 2011–02-18 measured by GOES15 (0.1–0.8 nm), LYRA [ch2-4(Zr)] (1–2 + 6–20 nm) and ESP (0.1–7 nm) (black, grey, and purple lines respectively). Simultaneous VLF amplitude (red) and phase (blue) lines for the NWC/19.8 kHz signal, recorded at Belgrade. (For interpretation of the references to colour in this figure legend, the reader is referred to the Web version of this article.)

2005-01-17 09:52 UT, though it has been registered on GOES only. Table 1 and Table 2 describe the observations for each flare: time of flare occurrence, $t(I_{max})$, irradiance peak value, I_{max}, as registered by GOES, ESP and LYRA, time of VLF extreme amplitude and phase perturbation, $t(A_{extr}, P_{extr})$, Tx and Rx geographical coordinates, Tx to Rx distance along the Great Circle Path and the amplitude and phase time delay, Δt_A and Δt_P.

The following gives a brief overview of the measured datasets for the selected flare events.

2.1.1. *Flares M9.4 2011-02-18 10:11 UT and M1.4 2011-02-18 14:08 UT*

The day of 2011–02-18 is characterized by intense solar flare activity, as reported by NOAA's Space Weather Prediction Center (SWPC), with 20 flares in close succession, mainly of class C. Fig. 2 shows the irradiances measured by GOES, ESP and LYRA in coincidence with VLF (A, P) measured in Belgrade for 06:00–11:30 UT when the *long* NWC-Bel path is completely sunlit. Four morning (UT) flares are VLF detected with distinct maximum in *both* (A, P). The largest is an M9.4 flare, with the amplitude peaking at 10:13 UT and the phase at 10:14 UT, i.e. after the peaks of the GOES (10:11 UT), the ESP and LYRA (10:12 UT) irradiance occur. Therefore, for the M9.4 flare on the NWC-Bel path we identify $\Delta t_A = 2$ min and $\Delta t_P = 3$ min, with respect to GOES irradiance and $(\Delta t_A, \Delta t_P)$, i.e. (1, 2) min with respect to ESP and LYRA irradiances (Table 1). After 13:00 UT more than half of the NWC-Bel path is unlit,

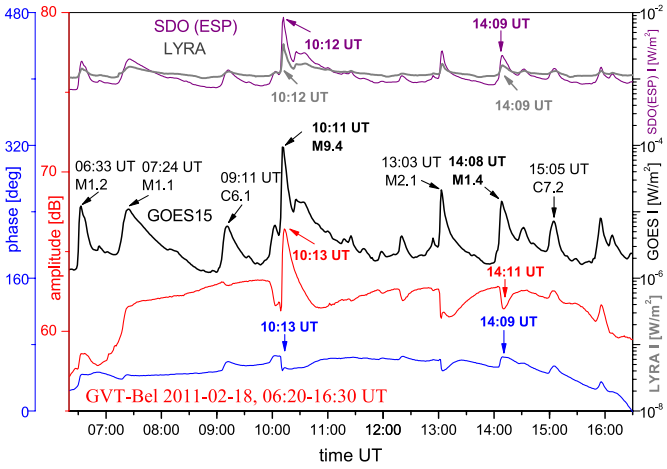

Fig. 3. Integrated Solar Irradiance (ISI) on the active day 2011–02-18 measured by GOES15 (0.1–0.8 nm), LYRA [ch2-4(Zr)] (1–2 + 6–20 nm) and ESP (0.1–7 nm) (black, grey, and purple lines respectively.); simultaneous VLF amplitude (red) and phase (blue) lines for the GVT/22.1 kHz signal, recorded at Belgrade. Flare class and UT of irradiance and VLF (A, P) peaks for the M9.4 flare at 10:11 UT and the M1.4 flare at 14:08 UT are indicated in bold font. (For interpretation of the references to colour in this figure legend, the reader is referred to the Web version of this article.)

and there are no VLF signatures of the UT afternoon flares on this path.

Fig. 2 is complemented by Fig. 3, displaying irradiance and VLF (A, P) timings on the same day, but with the VLF (A, P) recorded on the *short* GTV-Bel path. Measurements over the period 06:30–16:30 UT clearly show VLF signatures of the UT afternoon flares. It can be seen from Fig. 3 that a flare can induce different types of (A, P) time profile perturbations, either a maximum (M9.4) or a minimum (M1.4) in amplitude, or a preflare drop followed by the oscillation in either amplitude (M1.4) or in phase (M9.4). The M9.4 flare is studied on both NWC-Bel and GVT-Bel VLF paths with distinctly different (A, P) perturbation patterns, but which bring forth the *same* Δt_A (2 min for GOES; 1 min for LYRA and ESP), on both paths (Table 1). This makes the M9.4 flare a good candidate for comparing the $N(t, h)$ and LWPC approach. The M1.4 flare is associated with a minimum in amplitude and a maximum in phase, a pattern particular to low M-class flares on the short VLF GVT (GQD)/22.1 KHz - Bel path (Grubor et al., 2008).

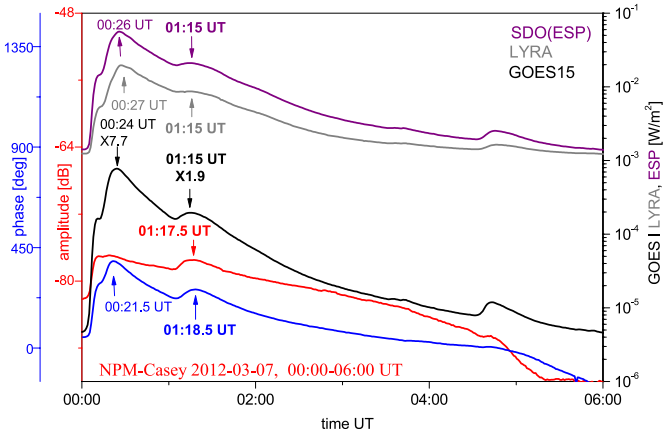

Fig. 4. Integrated Solar Irradiance (ISI) on the active day 2012–03-07 measured by GOES15 (0.1–0.8 nm), LYRA [ch2-4(Zr)] (1–2 + 6–20 nm) and ESP (0.1–7 nm) (black, grey, and purple lines respectively); simultaneous VLF amplitude (red) and phase (blue) lines for the NPM/21.4 kHz signal, recorded at Casey, Antarctica. For the X7.7 flare at 00:24 UT, $\Delta t_A < 0$ and $\Delta t_P < 0$ are apparent. (For interpretation of the references to colour in this figure legend, the reader is referred to the Web version of this article.)

2.1.2. Flares X7.7 2012-03-07 00:24 UT and X1.9 2012-03-07 01:15 UT

Fig. 4 presents time profiles of irradiance, according to GOES, ESP and LYRA, and the VLF signal for 2012-03-07. The strong X7.7 and X1.9 flares have clear VLF responses, maximum in both (A,P) on the completely lit path NPM/21.4 kHz - Casey, Antarctica (local time = UT+8 h). The XUV and EUV flare emissions, monitored by ESP and LYRA regularly peak after the XRS signal of GOES, as they correspond to a cooler temperature of emission, and therefore usually peak when the high temperature emissions induced by the flare process have already significantly decreased (Dolla et al., 2012; Benz, 2017). However, the X1.9 flare is distinguished, in particular, by an irradiance maximum recorded as simultaneous, at 01:15 UT, by all three space instruments GOES, LYRA and ESP. This renders *one value* of Δt_A (*one value* of Δt_P), regardless of the instrument in question. As each instrument bandpass can be associated to a specific temperature range of the emitting plasma, the simultaneous appearance of the X1.9 flare peak according to the three instruments indicates a very fast heating of the solar plasma in the flaring region. The strong X7.7 class flare is specific for its spectral components, being detected also by the Fermi Large Area Telescope in the gamma-ray wavelength range with energies >100 MeV. At the time, the X7.7 flare was the highest energy flare ever associated with the eruption on the Sun (Ajello et al., 2021). The peaking of the respective (A,P) before the irradiance peak as recorded in the (0.1–0.8) nm range, gives $\Delta t_A < 0$ and $\Delta t_P < 0$, which is physically unacceptable for the $N(t,h)$ model and negates further consideration of the X7.7 flare within the limitations of this study. It is possible that a positive time delay might be found for the extreme X7.7 flare if the hard X-ray irradiance datasets were included in the analysis (Briand et al., 2022).

2.1.3. Flare X5.5(X5.9) 2005-01-17 09:52 UT

The 2005-01-17 09:52 UT X5.5 (X5.9) flare, registered by GOES only, (at the time SDO and PROBA2 were not yet been launched), is taken into consideration, as it belongs to a series of strong eruptive events in January 2005, which have received much research attention (e.g. Osepian et al., 2009; Singer et al., 2011). Thus, the possibility of comparing the present results with other independent sources addressing the same event is highly significant. Fig. 5 presents the irradiance measured by GOES12, with the X5.5 flare registered at 09:52 UT, and by GOES10 with a somewhat higher maximal value, (class X5.9), with equal values at 09:52 and 09:53 UT, (which might be a saturation of the instrument). For evaluations (with interpolation functions) the maximum of I (GOES10) was taken at 09:52:30 UT. The simultaneous (A,P) variations on the NAA-Bel path are also shown in Fig. 5. The prominent solar flare

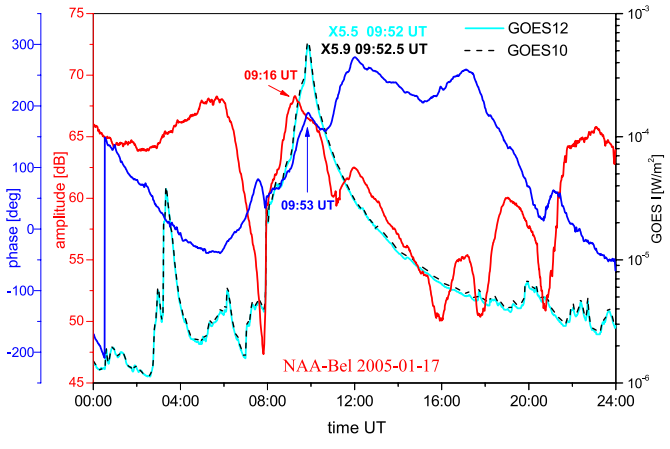

Fig. 5. Integrated Solar Irradiance (ISI) on the active day 2005–01-17 measured by GOES satellites (0.1–0.8 nm); GOES10 (black dashed line) and GOES12 (cyan line). Simultaneous VLF amplitude (red) and phase (blue) lines for the NAA/24.0 kHz signal, recorded at Belgrade. $\Delta t_A < 0$ is evident. (For interpretation of the references to colour in this figure legend, the reader is referred to the Web version of this article.)

was preceded by two fast Halo CMEs in close succession and followed by a steep rise of solar proton fluxes (NOAA SWPC). The X5.5 (X5.9) flare falls into the category of flares, associated with CMEs and Solar Proton Events (SPEs), and possibly also harder X-rays that apparently restrain the VLF amplitude growth and advance its maximum perturbation before the peak of the flare, $\Delta t_A < 0$ (e.g. Thomson et al., 2005). However, the VLF phase has a positive time delay $\Delta t_P > 0$ (0.5 and 1 min with respect to irradiances measured by GOES10 and GOES12 respectively).

3. Modelling ionization rate: methods and input data analysis

3.1. Basic procedure and equations

For each instrument, we evaluate the integral ionization rate (i.e. production rate) $q(t)$ [$m^{-3}s^{-1}$] for the selectively monitoring bandpass within the height range 55–100 km. *Monochromatic* irradiance I_{λ_i}, as measured outside the Earth's atmosphere, gives rise to ionization rate q_{λ_i} at time t and at height h above Earth expressed as (Ohshio et al., 1966):

$$q_{\lambda_i}(t,h,\chi,\lambda_i) = k_{\lambda_i}(h,\chi,\lambda_i)\, I_{\lambda_i}(t,\lambda_i) \quad (i=1,2\ldots) \tag{1}$$

where χ is the solar zenith angle, k_{λ_i} is the *'Local* photoIonization Efficiency' (LIE), i.e. the number of electron-ion (e-i) pairs produced per unit energy of irradiance I_{λ_i} per unit path length. k_{λ_i} are consistent with the Chapman function (e.g. Ratcliffe, 1972) and are extended to take into account real neutral atmospheric species: O_2, N_2, O, NO, and Ar, their height distribution, and the species absorption and photoionization cross sections (Ohshio et al., 1966 and references therein). The total ionization rate q is then the integral of the monochromatic q_{λ_i} over the respective instrument bandpass, narrow for GOES and broader for LYRA and ESP. Therefore, we extend the summations suggested by Eq. (1) to an integral form and express the *integral* ionization rate ('ionization rate' for short), at time t and at height h (e.g. Ratcliffe, 1972; Budden, 1988), as:

$$q(t,h,\chi) = k(t,h)\, I(t)\cos\chi(t) \tag{2}$$

with the *integral* ionization efficiency, (hereafter 'ionization efficiency') k determined from the discrete LIE $k_{\lambda_i}(\lambda_i,h)$ values over the wavelength range of the bandpass of GOES, ESP and LYRA, measuring the ISI, $I(t)$. In Eq. (2), the dependence on χ , taken at ground level, is accounted for explicitly, so that $k_{\lambda_i}(\lambda_i,h)$ for vertical incidence of radiation ($\chi = 0$) is used in the evaluations.

In solar flare conditions, the ISI time series, $I(t)$, reveals the severe increase of the X-ray/EUV irradiance up to 2–3 orders of magnitude above the regular level, often within a few minutes and then the decay in times ranging from tens of minutes to hours (e.g. Figs. 2–5). Through $I(t)$ the ionization rate Eq. (2) clearly bears this prominent time dependence. The ionization efficiency k and the zenith angle χ, are also time-dependent, but to a much smaller extent, so they are taken at the peak of the flare, i.e. at $t_{I_{max}}$..

Consequently, the height-dependent ionization efficiency, $k(h)$, for each instrument bandpass and for *each* particular flare is defined at the peak of the flare, (at $t_{I_{max}}$) as:

$$k(h) \equiv k(h,t_{I_{max}}) = \frac{\int_{\lambda_1}^{\lambda_2} k_\lambda(\lambda,h)\, I_\lambda(\lambda,t_{I_{max}})d\lambda}{I_{INST.}(t_{I_{max}})}\,. \tag{3}$$

Here $k_\lambda(\lambda,h)$ [$J^{-1}m^{-1}$] is the local ionization efficiency (LIE) and, $I_\lambda(\lambda)$ [$Wm^{-2}nm^{-1}$] is the Solar Spectral Irradiance (SSI), both of these are *functions* taken over the wavelength range corresponding to the instrument bandpass. The subscript in $I_{INST.}$ emphasizes ISI as an instrument measured quantity, in contrast to other quantities in Eq. (3) which include physical and numerical modelling. The wavelengths λ_1 and λ_2, are the bandpass boundaries of the GOES, ESP and LYRA sensors measuring the respective $I_{INST.}$.

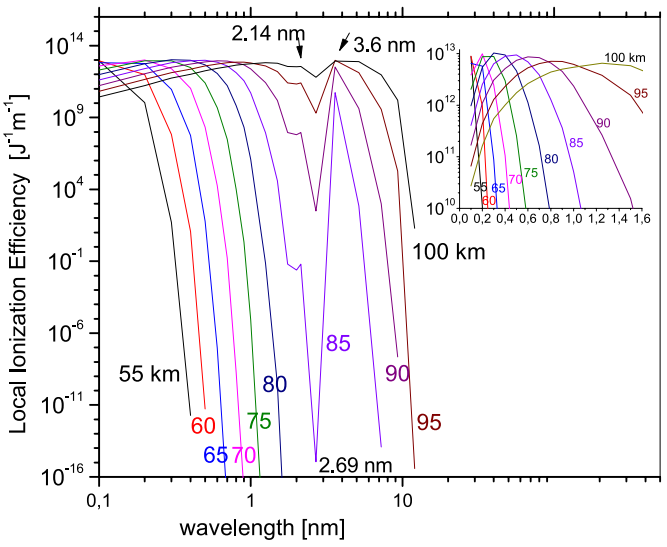

Fig. 6. Local Ionization Efficiency (LIE) [J^{-1} m^{-1}], Ohshio et al., 1966, for wavelengths 0.1–12.05 nm and heights 55–100 km. The inset displays the 0.1–1.6 nm region.

3.2. Local ionization efficiency data

For $k_\lambda(\lambda, h)$ use is made of the extensive work of Ohshio et al. (1966), which gives LIE data spanning 30–300 km in altitude and 0.01–137.5 nm in wavelength. Fig. 6 shows LIE, $k_{\lambda_i}(\lambda_i, h)$, in units number of e-i pairs per unit energy per unit length [J^{-1} m^{-1}], within the *effective* ionization bandpass (0.1, 12.05) nm, for heights of 55–100 km. The inset in Fig. 6 is a close up of the (0.1, 1.6) nm domain. The common nominal bandpass of the instruments extends from 0.1 to 20 nm. However, for a given height, after reaching the maximum, LIE has decreasing tendency with increasing wavelength, so that at every height there is a 'cut-off' wavelength beyond which LIE falls to zero. Therefore, there is an upper limit to the wavelength domain relevant for ionization, at each height. This *ionization effective bandpass* widens with height, extending to at most 12.05 nm for altitudes of 55–100 km. The altitude resolution is 5 km for all wavelengths considered.

In the sub-nanometer wavelength range the maxima in LIE curves are transferred to longer wavelengths with increasing heights (see inset in Fig. 6). Ionization is most efficiently produced by 0.1 and 0.2 nm, up to 70 km height, while wavelengths around 1 nm are most effective for ionization at 100 km.

A severe decrease of LIE between 2.14 and 3.6 nm, for heights of 85–100 km with the minimum at ~2.7 nm, is most likely due to the significant drop of absorption and photoionization cross sections between 1 and 10 nm for long-living oxygen atoms which reach their maximum concentration at these heights (Enell et al., 2011). Further contribution to the LIE minimum comes from the comparable drop in the absorption cross sections of O_2 and of N_2 which dominate at these heights (e.g. Whitten and Poppoff, 1965; Hargreaves, 1992).

3.3. Solar spectral irradiance data. The XUV Photometer System (XPS) algorithm

For the SSI, I_λ , we have considered several models: including CHIANTI (Dere et al., 1997; Landi et al., 2012) and the Flare Irradiance Spectral Model (FISM) (Chamberlin et al., 2008) and chose the XUV Photometer System (XPS)-Level 4 data product (Woods et al., 2008, 2012), due to its suitable spectral resolution (0.1 nm) and wavelength coverage (0.1–40 nm) such that the nominal bandpasses of GOES, ESP and LYRA are safely covered. The XPS-Level 4 data product uses the CHIANTI models of spectral irradiance in various states of solar activity to correct the broadband measurements by both XPS instruments onboard the Solar Radiation and Climate Experiment (SORCE) and Thermosphere, Ionosphere, Mesosphere, Energetics, and Dynamics (TIMED) satellites. Since 2020, a new version of FISM, named FISM2 (Chamberlin et al., 2020) is available, which is based on more recent measurements, in particular by the SDO/EVE, the SORCE/XPS and SORCE/Solar Stellar Irradiance Comparison Experiment (SOLSTICE). This new version, which provides the same resolution as the XPS-Level 4 used presently, was not available at the time of this work, but might constitute an interesting alternative to XPS-Level 4.

There is a one-to-one correspondence between the generated XPS SSI and a particular flare event under study. One difficulty that arises in this procedure is that the reproduction of XPS SSI at the time of the *flare peak* is not always possible, (Woods et al., 2008, 2012), in which case the SSI closest to flare peak is chosen. To overcome this deficiency, in evaluating $k(h)$, we combine modelled and observational data and take the instrument measured value $I_{INST.}$ in Eq. (3) at the time, τ, of the modelled spectral irradiance, $I_\lambda^{(XPS)}(\lambda, \tau)$, availability.

Insight into the 'goodness' of the XPS model can be gained by comparing both times $t_{I_{\max}}$ and τ, as well as the evaluated ISI, $I_{INST.}^{(XPS)}(\tau) (= \int_{\lambda_1}^{\lambda_2} I_\lambda^{(XPS)}(\lambda, \tau) d\lambda)$, and the measured $I_{INST.}(\tau)$. To this purpose, Table 3 lists flare class and irradiance peak time according to GOES (column 1); GOES measured peak irradiance ISI (SWPC scale factors removed) (column2); time τ of availability of the XPS SSI closest to the flare peak (column 3). The following columns show pairs of ISI, at time τ, as *evaluated* over the instrument bandpass, and as *measured,* by GOES, ESP and LYRA, respectively. It can be appreciated that at time τ, the following relations hold:

$$I_{GOES}(\tau) < I_{GOES}^{(XPS)}(\tau), \tag{4}$$

and contrary:

$$I_{ESP}(\tau) > I_{ESP}^{(XPS)}(\tau);\ I_{LYRA}(\tau) > I_{LYRA}^{(XPS)}(\tau) \tag{5}$$

The GOES measured ISI for the flares listed in Table 3 is less than the evaluated ISI by a factor that varies between 0.7 and 0.8. The ESP and LYRA measured ISI are greater than the evaluated ISI by factors 5.5 and 1.5 respectively for the M class flare, and factors of 13.2 and 4, (14.7 and 3.5) respectively for the X1.9 (X7.7) flare. It is apparent that the SSI according to the XPS model is overestimated in the 0.1–0.8 nm range and on the contrary significantly underestimated in the 1–15 nm range, as commented by Woods et al. (2008).

Fig. 7 illustrates the high variability of the time-resolved XPS -Level 4 SSI in the 0.1–20 nm, for the flares studied presently. It is to be noticed that the time τ of the XPS SSI, indicated in Fig. 7 coincides with the time of the flare peak $t_{I_{max}}$, as detected by GOES, for two flares only: the X5.5 flare (Table 2, column 3) and the X1.9 flare (Table 3, column 1). On 2011-02-18, the SSI for the M1.4 flare is given at the ESP and LYRA ISI maximum (14:09 UT), near to the GOES maximum (14:08 UT), while the SSI for the M9.4 flare is produced at 10:30 UT, at the decaying phase of the M9.4 flare (GOES ISI peaking at 10:11 UT). This results in XPS SSI curves for the M9.4 and M1.4 flares, which refer to *different* phases of two flares, but are strikingly similar, as can be appreciated from Fig. 7.

The XPS model, like any computational algorithm, has its limitations. Flares are indeed highly individual events and their pronounced variability shows dependence not only on the strength, but as well on the spectral composition and on the temporal evolution (e.g. Aschwanden et al., 2015). Because of the dependence on these properties that are intrinsic to a particular flare, the same XPS algorithm may work better for some flares than for others, as illustrated by the example of the flare 2005 - 01–17 09:52 UT X5.5 (X5.9) and detailed in Section 5.3.

Table 3
Measured and calculated Integrated Solar Irradiance, I, for flares simultaneously observed by GOES, ESP and LYRA

GOES Flare Class Flare peak time (yyyy-mm-dd hh:mm) UT	$I_{GOES}(t_{I_{max}})$ [Wm^{-2}]	τ hh:mm UT	$I^{(XPS)}_{GOES}(\tau)$ [Wm^{-2}]	$I_{GOES}(\tau)$ [Wm^{-2}]	$I^{(XPS)}_{ESP}(\tau)$ [Wm^{-2}]	$I_{ESP}(\tau)$ [Wm^{-2}]	$I^{(XPS)}_{LYRA}(\tau)$ [Wm^{-2}]	$I_{LYRA}(\tau)$ [Wm^{-2}]
M9.4 2011-02-18 10:11	9.44057 10^{-5}	10:30	1.96498 10^{-5}	1.39119 10^{-5}	4.34528 10^{-4}	0.0024	0.0011	0.00165
M1.4 2011-02-18 14:08	1.43786 10^{-5}	14:09 (*)	1.69885 10^{-5}	1.36854 10^{-5}	4.00676 10^{-4}	0.0023 (*)	0.00106	0.00161 (*)
X7.7 2012-03-07 00:24	7.75714 10^{-4}	00:13	2.35739 10^{-4}	1.87143 10^{-4}	0.00106	0.0156	0.00155	0.0055
X1.9 2012-03-07 01:15	1.95714 10^{-4}	01:15 (*)	2.56484 10^{-4}	1.95714 10^{-4} (*)	0.0016	0.0211 (*)	0.00216	0.00869 (*)

(*) Indicates that for a particular instrument the times τ and t_{Imax} coincide or are very close and therefore $I(\tau)$ and I_{max} practically coincide.
Measured and calculated ISI for the flares studied. The first column identifies the flare by its class in GOES scale, and peak time, $(t_{I_{max}})$. The next columns respectively provide the (corrected) peak irradiance measured by GOES $(I_{GOES}(t_{I_{max}}))$, the time (τ) of the XPS spectrum $(I^{(XPS)}_{\lambda})$, the XPS spectrum integrated over the GOES bandpass $(I^{(XPS)}_{GOES}(\tau))$, the (corrected) irradiance measured by GOES at time τ, $(I_{GOES}(\tau))$, the XPS spectrum integrated over the ESP bandpass $(I^{(XPS)}_{ESP}(\tau))$, the irradiance measured by ESP at time τ , $(I_{ESP}(\tau))$, the XPS spectrum integrated over the LYRA bandpass $(I^{(XPS)}_{LYRA}(\tau))$ and the irradiance measured by LYRA at time τ $(I_{LYRA}(\tau))$.

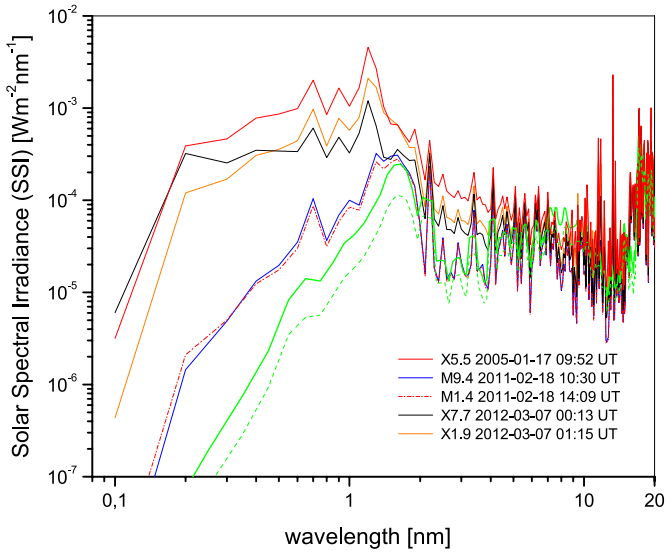

Fig. 7. XPS-Level 4 Solar Spectral Irradiance, SSI, $(I^{(XPS)}_{\lambda})$, in the range of 0.1–20 nm (Woods et al., 2008). The time τ of the generation of the XPS spectra is indicated in the figure. Daily averaged TIMED/SEE SSI is presented by green lines, dashed for the quiet day 2011–02-22 and solid for the active day 2012–03-07. (For interpretation of the references to colour in this figure legend, the reader is referred to the Web version of this article.)

4. Modelling electron densities during solar flares

4.1. The N(t, h) model – solving the electron continuity equation

The three-component (electrons, positive and negative ions) hydrodynamic model with global electroneutrality taken into account and diffusion neglected on timescales of event duration, leads to the electron continuity equation which describes the temporal-height evolution of the electron density N resulting from concurrent electron production (ionization rate q) and electron loss processes, α being the effective recombination coefficient:

$$\frac{dN(t,h)}{dt} = q(t,h) - \alpha(h)N^2(t,h)\ . \tag{6}$$

Equation (6) has been commonly used for D-region studies. It is traditionally used under the assumption of steady state, $\frac{dN}{dt} = 0$ to infer effective recombination coefficients for a broad variety of space weather events like solar flares (Ananthakrishnan et al., 1973), electron precipitation (Collis et al., 1996), and SPEs (e.g. Osepian et al., 2009), or by assuming $q = 0$, to study e-i kinetics from relaxation processes (e.g. Rodger et al., 1998). More recently, Eq. (6) has been solved by taking a plausible time dependence for the ionization rate, when periodicities in the electron content and in the radio absorption have been observed (Hargreaves and Birch, 2018).

In the present study we solve the *time-dependent* continuity Eq. (6), with ionization rate q, Eq. (2), taken as directly proportional to the dominant flare irradiance, using the respective X-ray and EUV ISI time series $I_{INST.}(t)$, as *measured* by space instruments.

This approach, designated as the $N(t,h)$ model, is an updated version of the $N(t)$ model that has been put forward by (Žigman et al., 2007) and has since been applied to a large number of flares detected by the VLF Belgrade receiver (e.g. Grubor et al., 2008). Within the $N(t)$ model the ionization efficiency was assessed semi-empirically from ionization rates estimated at diverse flare conditions, confined to a limited range of heights, as reported in the literature (e.g. Allen, 1965; Rishbeth and Garriott, 1969; Osepian et al., 2009), which likely introduced fairly large uncertainties when applied to highly variable flare events. In this study, we aim at circumventing this difficulty by modelling the ionization efficiency using the XPS SSI, and by relating a specific ionization rate to each flare event as detected within the wavelength coverage of the particular instrument.

One advantage of the $N(t,h)$ model is the possibility to deduce the effective recombination coefficient α within the model itself by recognizing the importance of the time delay. The extreme VLF amplitude (and phase), delayed with respect to the flare peak, coincide with the flare induced maximal enhancement of electron density (McRae and Thomson, 2000; Grubor et al., 2008). Therefore, the time delay of the extreme amplitude and/or phase value with respect to the X-ray/EUV flare peak is as well the time delay of the maximal electron density behind the flare peak (Žigman et al., 2007):

$$\Delta t = \left(t_{(A,P)_{extr.}} - t_{I_{max}}\right) \equiv \left(t_{N_{max}} - t_{I_{max}}\right). \tag{7}$$

The effective recombination coefficient α is connected to the *time delay*, i.e. the time shift of maximum density, N_{max}, with respect to the flare peak irradiance, I_{max}, by the Appleton relation (Appleton, 1953), presently applied to the active ionosphere:

$$\left(t_{N_{max}} - t_{I_{max}}\right) \equiv \Delta t = \frac{1}{2\alpha N(I_{max})}\ . \tag{8}$$

Required *equality* between the maximum electron density N_{max} as deduced from Eq. (6) and as expressed through the temporally close electron density at maximum irradiance, (I_{max}) , Eq. (8), imposes a constraint demanding the constancy of the product $k(h)\alpha(h)\cos\chi$, namely:

$$k(h)\alpha(h)\cos\chi = \textit{flare const.} = F\left(I_{\max}, I\left(t_{(A,P)_{\text{extr.}}}\right), \Delta t\right) . \quad (9)$$

(For details see Eqs. (14-16) in Žigman et al., 2007). As indicated, in Eq. (9), the value of 'flare const.' [$m^2J^{-1}s^{-1}$] is subject to the flare characteristic observables: $I_{\max}$, either $I(t_{A_{\text{extr}}})$ or $I(t_{P_{\text{extr}}})$ and time delay Δt, and as such is *unique* to each flare event. With $k(h)$ evaluated according to Section 3, one can infer the corresponding effective recombination coefficient $\alpha(h)$ from Eq. (9).

With both $k(h)$ and $\alpha(h)$ assigned to a particular flare, Eq. (6) is solved for the time interval determined by the *beginning* and *end* of the flare event, as reported by the GOES Event Lists (ftp://ftp.swpc.noaa.gov/pub/warehouse/yyyy/yyyy_events.tar.gz). In some cases, the lower limit of the time interval is extended (by a few min at most), to capture the flare *effect* on the VLF (A,P), i.e. to the instant when both (A,P) clearly start to *follow* the increase of the flare intensity. If the flare under study is not followed by another one, the upper limit of the time interval can be extended deliberately, to compare the relaxation in $I(t)$ and the resulting $N(t,h)$.

One can argue that there is no need to solve Eq. (6), since $N_{\max}$ can be easily deduced from $(dN/dt = 0)_{N_{\max}}$. However, time delay is needed to obtain $I(t_{N_{\max}})$ i.e. $I\left(t_{(A,P)_{\text{extr}}}\right)$ in Eq. (9), whereas the Appleton relation Eq. (8) necessitates the value of $N(t_{I_{\max}}) \equiv N(I_{\max})$.

Here, with the $N(t,h)$ solution of Eq. (6) we reconstruct the continuous time behaviour of the electron density throughout the flare event, as this is recorded by instruments onboard GOES, ESP and LYRA and simultaneously VLF detected on different Tx to Rx paths (Tables 1 and 2). The results apply to the altitude range of 55–100 km with a height resolution of 5 km.

It is important to note that by solving Eq. (6) the *evaluated time delay* Δt_{ev} is obtained. Comparison with measured Δt provides a criterion for the validity of the model. Furthermore, starting from some physically reasonable value of the effective recombination coefficient, Δt_{ev} can be used as a parameter optimizing the value of α through a 'trial and error' iterated solving of Eq. (6).

4.2. The long wave propagation model and code (LWPC)

The VLF experimental technique is a powerful tool, in large part, because it is supported by theory and the set of versatile programmes for simulation of VLF propagation. The Long Wave Propagation Code (LWPC), developed by the Naval Ocean System Center (NOSC) (Pappert and Snyder, 1972; Ferguson and Snyder, 1990) has an acknowledged history of improvements (Ferguson, 1998)and is currently used by the ionospheric research community as a benchmark for extension of VLF propagation codes (e.g. Xu et al., 2021). Much like the VLF experimental technique detects, the accompanying LWPC evaluates ionization changes in the D-region regardless of their driving agent (e.g. Žigman et al., 2014).

The most widely used LWPC model for the D-region is the so called 'Wait two-parameter ionosphere' with two parameters: the ionospheric 'sharpness' β [km^{-1}] and the reference (also termed 'reflection') height H' [km], which together determine the calculated VLF (A,P) in the simulation routine (Wait and Spies, 1964). The sharpness β of the ionosphere lower boundary gives the relative slope of the conductivity/electron density profile. The parameter H' is the altitude at which the reflection of the VLF waves takes place. At disturbed ionospheric conditions the programme is run in a 'trial and error mode', by performing iterations starting from regular or well guessed (β, H') pairs until the modelled (A,P) match those observed. The resulting agreement yields β and H' appropriate to the perturbed D-region. The general behaviour of the pair (β, H') in flare conditions is well-established through numerous LWPC studies: increased flare irradiance results in increased sharpness β and lowered reflection heights H' (e.g. Thomson et al., 2005).

From the general dispersion equation for (VLF) waves in a weakly ionized, electron-neutral *collision-dominated* plasma as is the D-region (e.g. Budden, 1988), and assuming exponential decrease of neutral density with height, the electron density profile $N(h)$ [m^{-3}], is furnished as a function of the LWPC parameters β and H' (Wait and Spies, 1964; Thomson, 1993):

$$N(h, H', \beta) = 1.43\ 10^{13} \exp(-0.15\, H') \exp[(\beta - 0.15)(h - H')] \quad (10)$$

Presently, we use the standard LWPC v2.0 (Ferguson, 1998) to validate the results of the $N(t,h)$ method. The code yields pairs of (A,P) and (β, H') and the electron density height profile, Eq. (10), at a given time, usually chosen as the time extremes were observed in the amplitude or phase values, since maximum changes are of primary concern in flare studies. However, the model can be time-resolved by applying the code to any of the (time-continuous) amplitude and phase measurements including the impulsive and the decay phase of the flare (Grubor et al., 2008). Along this line, we apply the LWPC, at the *beginning* of the flare event to simulate the corresponding (A,P), and by inferring the (β, H') pair, to evaluate the initial or *pre-flare* electron density N_0, needed for solving Eq. (6). This procedure is required when the LWPC default 'quiet' electron density is not suitable for the already disturbed preflare ionosphere and in some cases, needs extending the lower limit of the time-interval of flare appearance, determined by the GOES event lists, as commented in Section 4.1.

5. Evaluations and results

5.1. Ionization efficiency

The ionization efficiency, $k(h)$, over the bandpass of the instruments and in the height range 55–100 km, evaluated according to Eq. (3), is presented in Fig. 8 for the flares studied as registered by GOES, ESP and LYRA.

The $k(h)$-curves pertaining to a particular instrument are grouped together, evidencing distinction between instruments' bandpass ranges. The general increasing trend of k with both height and flare irradiance is apparent for both ESP and LYRA throughout the height range

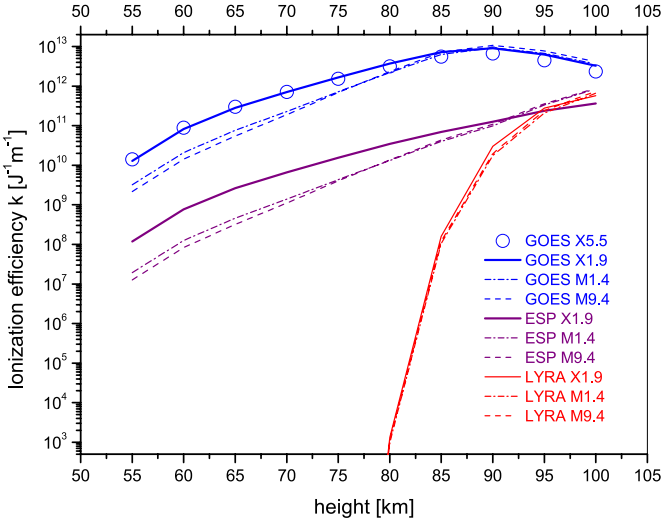

Fig. 8. Ionization efficiency for 55–100 km altitude for the flares X1.9 2012-03-07 01:15 UT, M9.4 2011-02-18 10:11 UT, M1.4 2011-02-18 14:08 UT, represented by line colour: blue for GOES, purple for ESP and red for LYRA; line styles: solid for X1.9, dashed for M9.4 and dash-dotted for M1.4. Circles refer to the flare X5.5 2005-01-17 09:52 UT registered by GOES only. The XPS SSI is generated for each particular flare at time τ [FlareClass(τ)]: X5.5 (09:52 UT), X1.9 (01:15 UT), M9.4 (10:30 UT), M1.4 (14:09 UT). (For interpretation of the references to colour in this figure legend, the reader is referred to the Web version of this article.)

considered, and for GOES up to 90 km, where the GOES bandpass k reaches a maximum. This property of the ionization efficiency and hence of the ionization rate in the soft X-rays is well known (e.g. Hargreaves, 1992). Above 90 km the ionization efficiency of the 0.1–0.8 nm band declines and longer wavelengths above 1 nm 'take over' the ionization at higher heights (Fig. 6). This is manifested by the convergence of the ESP and LYRA $k(h)$-curves at above 90 km height. Since below 0.3 nm the SSI for the M1.4 flare at maximum is higher than for the M9.4 flare at the decaying phase (Fig. 7), so are the respective $k(h)$ values below 75 km (Fig. 8), indicating that the ionization by soft X-rays plays a dominant role at the lowest heights.

It is also evident from Fig. 8 that k-curves for GOES and ESP pertaining to the same flare, run almost in parallel from 55 km, up to some 75–80 km height, a result of the common ionization effective bandpass for GOES and ESP at these altitudes.

Very low values of $k(h)$ for LYRA at 90 km and extremely low for altitudes below, are due partly to the underestimated XPS spectrum above 1 nm and partly to the LYRA bandpass which does not comprise the sub-nanometer range. Apparently, the ionization efficiency for the LYRA bandpass up to 90 km height is too low to produce ionization.

5.2. Effective recombination coefficient

The results for the effective recombination coefficient $\alpha(h)$, deduced from constraint, Eq. (9), are presented in Fig. 9. The overall range of α covers values from 10^{-14} to 10^{-9} [m^3s^{-1}], which roughly comprises both the lower and upper limiting profile of this quantity under most varied ionospheric conditions (Hargreaves, 2005). Since α behaves as k^{-1}, Eq. (9), a minimum is displayed for flares observed with GOES (0.1–0.8 nm).

Gledhill (1986) extensively reviewed the literature on α values in the height span 50–150 km, at different ionospheric conditions and found that daytime values of α during solar flares in mid-latitude regions do not differ significantly from those observed at polar latitudes. For α values from various sources, 302 data points incorporating polar cap

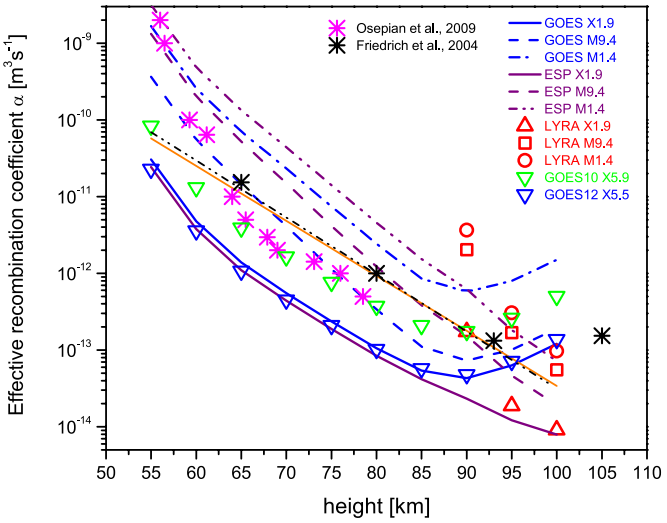

Fig. 9. Effective recombination coefficient at 55–100 km altitude for the flares X1.9 2012-03-07 01:15 UT, M9.4 2011-02-18 10:11 UT, M1.4 2011-02-18 14:08 UT, represented by line colour: blue for GOES, purple for ESP and by red points for LYRA; line and points styles: solid lines and up triangles for X1.9, dashed lines and squares for M9.4 and dash-dotted lines and circles for M1.4. For the flare X5.5 (X5.9) 2005-01-17 09:52 UT down triangles blue (green). Least square fit on the 79 (h,α)-points for the flares X5.5, M1.4, M9.4 and X1.9, as recorded by GOES, ESP and LYRA: black dash-dot-dotted line. Other sources: orange solid line - Gledhill (1986); asterisks: magenta - Osepian et al. (2009); black - Friedrich et al., 2004. (For interpretation of the references to colour in this figure legend, the reader is referred to the Web version of this article.)

absorption, sudden phase anomaly, SPEs, and solar flares, Gledhill performed a least squares fit and reported an exponential decrease of α [$m^3\ s^{-1}$] with height h [km]. The Gledhill α-profile:

$$\alpha_{\text{Gledhill}} = 5.01\ 10^{-7}\ \exp(-0.165\ h)$$

(shown as a solid orange line in Fig. 9) runs across the middle region of our α data. Indeed, analogous best-fit on the 79 (h,α)-points for the flares analyzed presently (M1.4, M9.4, X1.9 and X5.5), as recorded by GOES, ESP and LYRA, results in a strikingly similar regression line (black dash-dot-dotted in Fig. 9):

$$\alpha = 8.44\ \ 10^{-7}\ \exp(-0.171\ h) \tag{11}$$

giving a scale height of 5.8 km, in remarkable agreement with the Gledhill's, amounting to 6.1 km.

An estimate of the effective recombination coefficient at a given height, relies on Eq. (6) taken at $t_{N_{\max}}$; if both the ionization rate and the associated electron density are known, $\alpha(h)$ follows directly:

$$\alpha(h) = q(h)/N_{\max}^2\ . \tag{12}$$

Enhanced ionization rates of similar intensity, irrespective of their particular origin, are likely to produce similar electron density enhancements.

High latitude daytime effective recombination rates obtained by Friedrich et al. (2004) were inferred from electron densities obtained from 49 rocket-born radio propagation experiments and from ionization rates from measurements of particle fluxes and X-rays data from literature. Their reported mean recombination coefficients, modelled by a root mean square fit to the data, are presented in Fig. 9 at four heights (black asterisks). It is interesting to note that the Friedrich et al. (2004) mean α values closely follow both the Gledhill's and the present regression line, in the height range 60–95 km, though an enhancement in α is noticed at 105 km.

Osepian et al. (2009) have modelled the electron density and the ionization rate for the 2005-01-17 event, at 09:50 UT, at the latitude of Tromsø (69.6° N), deducing α values from Eq. (12). With the ionization rate for protons at Tromsø, higher than that of the X5.9 flare at mid-latitudes (Belgrade, ~44.8° N), Osepian et al. found recombination coefficients (magenta asterisks) that are somewhat higher, but in the altitude range of ~62–80 km still in good agreement with our results (green down triangles) for the X5.9 flare as observed on the NAA-Bel path.

5.3. Electron density time-height profile

With $k(h)$ and $\alpha(h)$ provided, the electron density time-height profiles are obtained by solving Eq. (6) as described in Section 4. For the M9.4, M1.4 and X1.9 flares the amplitude time delay, Δt_A, is employed, as measured for the specified VLF paths (Table 1).

The results of the $N(t,h)$ method for the maximal flare induced electron density $N_{\max}$ as a function of height, are presented by points in Fig. 10, considering the bandpass of the GOES, ESP and LYRA instruments for the (a) M9.4, (b) M1.4 and (c) X1.9 flares respectively. The increasing trend of $N_{\max}$ with height, similar to the trend observed for k (Fig. 8) is apparent. The GOES predicted $N_{\max}$ values go through the maximum at around 90 km height, as does the respective k (and eventually q).

It is apparent that the flare irradiance maximum, $I_{INST.}(t_{I_{\max}})$, strongly dominates the flare induced electron density enhancement; though the XPS SSI curves for the M9.4 and M1.4 flares are particularly close (Fig. 7), the $N_{\max}$ values are approximately one order of magnitude larger for M9.4 than for M1.4, regardless of the instrument considered, as seen from Fig. 10, (panels a and b).

For LYRA, the only results that are physically acceptable are those at and above 90 km height; $N_{\max}$(LYRA) approaching $N_{\max}$(ESP) at the highest altitudes, 95 and 100 km.

Evaluations of electron density throughout the considered height range, as pertaining to the bandpass ranges of the three instruments, are in best accordance for the X1.9 flare. This is likely due to the consistency of the time variation in the wavelength dependent solar flare irradiances. For this X1.9 *flare irradiances* measured by GOES, ESP and LYRA *peak simultaneously,* i.e. the time delays Δt_A (2.5 min), and Δt_P (3.5 min), are the *same* in the three instances (Table 1). In the height range of the GOES and ESP common ionization bandpass (up to 75 km), N_{max}(GOES) and N_{max}(ESP) for X1.9 (Fig. 10 c) are particularly close: N_{max}(ESP) = 1.18 N_{max}(GOES) which is well ascribed to equal Δt_A.

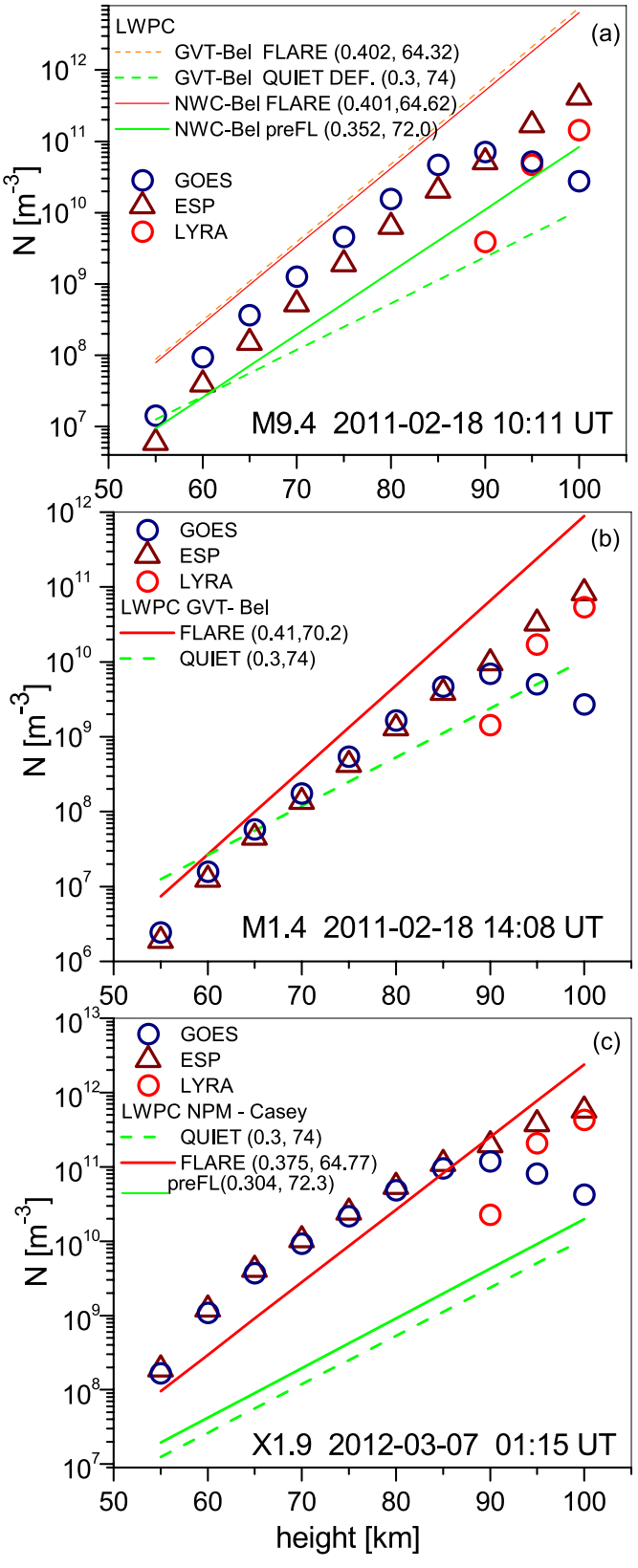

Fig. 10. Maximum flare induced electron density N_{max} height-profile. $N(t,h)$ model - points: according to irradiance measured by GOES (blue circles), ESP (purple triangles) and LYRA (red circles) and to the respective VLF Δt_A. VLF propagation LWPC model – lines: red for N_{max}, green for electron density at quiet and preflare conditions. The corresponding (β, H') ([km-1, km]) pairs are indicated in the legend of each panel. Panel (a) refers to the M9.4 2011-02-18 10:11 UT flare, with the VLF Δt_A equal for both signals NWC/19.8 kHz and GVT/22.1 kHz as received at Belgrade; $N(t,h)$ gives one $N_{max}(h)$ profile; LWPC, according to different (A,P) perturbations on the two paths gives two close profiles (solid red and dashed red lines). The green LWPC lines refer to the quiet state (dashed line) for the GVT signal and to the pre-flare state (solid line) for the NWC signal. Panel (b) refers to the M1.4 2011-02-18 14:08 UT flare, with the VLF Δt_A for the GVT/22.1 kHz signal as received at Belgrade. The green dashed LWPC line refers to the quiet state. Panel (c) refers to the X1.9 2012-03-07 01:15 UT flare, with the VLF Δt_A for the NPM/21.4 kHz signal as received at Casey. The green LWPC lines refer to the quiet state (dashed line) and to the pre-flare state (solid line). (For interpretation of the references to colour in this figure legend, the reader is referred to the Web version of this article.)

Above 90 km, N_{max}(LYRA) and N_{max}(ESP) show reasonable agreement for both the M1.4 (Fig. 10 b) and X1.9 (Fig. 10 c) flares. The comparison is not so favourable for the M9.4 flare, but one has to bear in mind that XPS SSI for the M9.4 flare actually refers to the far post-flare phase (τ = 10:30 UT).

Electron density height profiles, according to the LWPC routine, Eq. (10), at either quiet (i.e. normal daytime), or pre-flare and flare conditions are presented by lines in Fig. 10. The respective (β, H'), ([km^{-1}, km]), parameters are given in the legend. The N_{max}(LWPC) values, presented by red lines are simultaneous with the $N(t,h)$ results.

The default N(LWPC) height profile for the unperturbed, daytime, i. e. 'quiet' ionosphere (β = 0.30 km^{-1}, H' = 74.0 km), is presented where applicable (e.g. flare M1.4, Fig. 10 b). However, if a flare under study, like the X1.9 flare, is preceded by a larger flare (X7.7), which already significantly disturbs the ionospheric background, then the state of the ionosphere at the beginning of the flare in question is more adequately described by the pre-flare LWPC height profile, as presented in Fig. 10 c. These N(LWPC) values are also used in the $N(t,h)$ method as a benchmark for estimating the *initial* electron density (N_0) needed to solve the continuity equation. A limitation of the LWPC model (and of the VLF technique) is that reliable predictions of N are confined to the height range of some 60–90 km. Below and above these limits LWPC is likely to either underestimate or overestimate N. At those altitudes, N_0 needs to be iteratively adjusted.

The M9.4 flare, in particular, is detected on two VLF paths, NWC-Bel and GVT-Bel (Figs. 2 and 3). Therefore, two independent pairs of perturbed VLF (A,P) data, related to these paths, have been used to infer the flare induced N_{max}, as described by two LWPC height profiles, with two pairs of (β, H') (red lines in Fig. 10 a). The VLF amplitude peaks *simultaneously* at 10:13 UT, *on both paths*: NWC-Bel and GVT-Bel (Section 2, Table 1), providing equal time delay, Δt_A, for the M9.4 flare in both instances. Therefore, the $N(t,h)$ method yields *equal* electron density results, irrespectively of the VLF path, this being either NWC-Bel or GVT-Bel. This finding is strongly confirmed by the corresponding LWPC red lines, solid for the NWC-Bel and dashed for the GVT-Bel path, with remarkably similar values of N_{max} (LWPC), on the whole height domain, the discrepancies amounting from 10% to at most 14%.

Fig. 11 presents the $N(t,h)$ results for the 2005-01-17 09:52 UT flare. Registered simultaneously by GOES10 (green triangles) as of class X5.9 and by GOES12 (blue triangles) as of class X5.5, this flare pertains to the extraordinary solar proton storm of January 2005, extending through

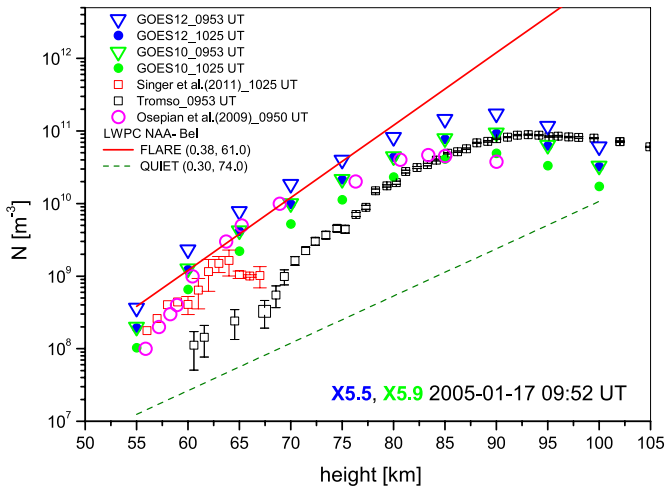

Fig. 11. Flare induced electron density N for the X5.5 (X5.9) 2005-01-17 09:52 UT flare. $N(t,h)$ model - points: according to the flare irradiance measured by GOES12 (X5.5): blue triangles - $N_{\max}$ at 09:53 UT, solid blue points - N, at 10:25 UT; and by GOES10 (X5.9): green triangles - $N_{\max}$ at 09:53 UT, solid green points - N, at 10:25 UT, and according to the respective VLF phase time delay for the signal NAA/24.0 kHz received at Belgrade. LWPC model: red line - $N_{\max}$ at 09:53 UT, dashed green line - quiet $N(h)$-profile. The corresponding (β, H') ([km^{-1}, km]) pairs are indicated in the legend. Observations: Singer et al. (2011) at 10:25 UT– red squares; Tromsø EISCAT-VHF radar at 09:53 UT – black squares. Model: Osepian et al. (2009) at 09:50 UT – magenta circles. (For interpretation of the references to colour in this figure legend, the reader is referred to the Web version of this article.)

days 15–22. The >10 MeV SPE starting on January 15 persisted up to midday January 17 when another SPE following the X5.5 flare and CME occurred, (NOAA Space Environment Services Center (SESC)).

When a proton event and a strong flare occur in close succession or simultaneously the VLF response to ionospheric changes is characterized by an amplitude that peaks before the flare irradiance attains its maximum value, i.e. the amplitude appears restrained/suppressed in its growth and starts decaying, while the flare flux is still in its impulsive phase (Fig. 5). Formally, this leads to the 'negative' amplitude time delay, which is physically inconsistent and as such not suited for the $N(t,h)$ approach. However, if the VLF phase maximal perturbation lags behind the flare peak irradiance, the respective (positive) phase time delay, Δt_P, can be used instead. This is the precisely the case of the X5.5 (X5.9) flare (Fig. 5), providing evidence of a successful deployment of Δt_P in the $N(t,h)$ method. Another advantageous point: the XPS SSI for the X5.5 (also valid for X5.9) is generated at the UT of the flare peak, i.e. $\tau \equiv t_{I_{\max}} =$ 09:52 UT which rules out the uncertainties that arise when this condition is not met. The agreement between the evaluated irradiance $I^{(XPS)}_{GOES}(t_{I_{max}})$ ($= 5.91\ 10^{-4}$ Wm^{-2}) and the measured one, $I_{GOES12}(t_{I_{\max}})$ ($= 5.51\ 10^{-4}$ Wm^{-2}), even better with GOES10, $I_{GOES10}(t_{I_{\max}})$ ($= 5.94\ 10^{-4}$ Wm^{-2}) is surprisingly good. It indicates the importance of reproducing the XPS-modelled SSI at the time of the flare maximum, as well as a smaller extent of the XPS SSI overestimation on the 0.1–0.8 nm bandpass for large, X-class, flares. Simultaneous measurements of the flare by GOES10 and GOES12 satellites allow the estimate of the error in ISI which is negligible, except at flare maximum where it amounts to around 3%.

In Fig. 11 it can be seen that according to $N(t,h)$, $N_{\max}(h)$ evaluated with the GOES12 (X5.5) irradiance is higher than with the GOES10 (X5.9) data, which is due to a larger time delay of the former ($\Delta t_P = 1$ min), (Žigman et al., 2007). The $N_{\max}$ profiles deduced from the respective irradiance of GOES12 and GOES10 may well set the lower and upper limits of the N variations during the event.

Also presented in Fig. 11 are the electron density measurements of the EISCAT Tromsø (69.58° N, 19.21° E) VHF radar (224 MHz), retrieved from the Madrigal database (Häggström, 2005) available at 09:53 UT, which coincides with the time of the maximum N, (i.e. maximum VLF phase). We also include the Doppler radar (3.17 MHz) measurements of N at Andenes Norway, (69.31° N, 16.12° E) on 2005-01-17 10:25 UT which have been analyzed and reported by Singer et al. (2011). Both sets of data apply to the high latitude region, so care should be taken when considering comparisons with the somewhat lower latitude analysis presented here. During storm enhanced solar radiation, *observations* of N clearly comprise all present ionization sources, due to both waves and particles. However, at latitudes of Tromsø (~69.9° N) and Andenes (~69.3° N) and at zenith angles $\chi \approx 90°$, the ionization rates of X-rays are significantly below those due to proton fluxes. The measured N data refer to the time span 09:53–10:25 UT, which encompasses apart from the X5.5 class flare, strong remnants of the January 16 proton storm and there is, following the X5.5 flare, an increasing proton flux building up to result in a major SPE on January 17 peaking at 17:50 UT (NOAA SESC).

Osepian et al. (2009) applied their theoretical D-region ionization-recombination model to the state of the high latitude ionosphere during the 2005-01-17 event, at 09:50 UT, to calculate the SPE induced ionization rate and N. Their results are shown in Fig. 11 (magenta circles) and relate reasonably to our N findings. The Osepian et al. modelled values and the Tromsø measurements clearly indicate a maximum in the $N(h)$ profile at around 83.4 and at 93.1 km height, respectively, also predicted by our model for the GOES bandpass and set at (about) 90 km height. Considering the 5 km height resolution of the present results, the agreement is reasonably fair.

Based on the Andenes radar measurements, Singer et al. (2011) electron density profiles present the average values from the differential absorption experiment. Their estimates of N refer to 10:25 UT (red squares) and are confined to a rather narrow height range of 56–67 km (Singer, 2012). We compare the Singer et al. values with those from the $N(t,h)$ approach, as this allows reconstruction of the N height profile at *any* time from the beginning to the end of the flare event. Thus, Fig. 11 along with the $N_{\max}(h)[\equiv N(t_{P_{\max}}, h)]$ profile according to both GOES10 and GOES12 flare irradiance, also presents the two respective height profiles at 10:25 UT, i.e. $N(10:25\ \mathrm{UT}, h)$, (solid green and solid blue circles). In the narrow height span between 56 and 65 km, the Doppler measured N values (red squares) are in best agreement with those modelled with the GOES10 irradiance ($\Delta t_P = 0.5$ min) as well as with those of Osepian et al. (2009).

The full strength of the $N(t,h)$ method lies in providing both the height and time profile of the flare induced electron density. This is illustrated in Fig. 12 by presenting the *time* variation of N at 90 km height, i.e. $N(t,90)$, yielding the time evolution of the electron density, throughout flare duration for the flares analyzed in this study. It is clearly evidenced how the electron density (full lines), remarkably follows the pattern of the flare flux (dashed lines), with a time lag corresponding to the *measured* amplitude or phase time delay. The *evaluated* and measured time delays, listed in Table 4, are generally in notable agreement, the relative error amounting to less than 8% for all the flares simultaneously detected by the three space instruments, and by VLF propagation. However, two exceptions are noticed: for the flares X1.9 as registered by LYRA and for X5.9 as registered by GOES10, the time delay error is increased to about 18% and 15% respectively.

6. Discussion

The findings in this study corroborate the inferences drawn by Gledhill (1986) that effective recombination coefficients during solar flares as observed at mid-latitudes do not differ notably from those pertaining to daytime high-latitude events, such as SPE and polar cap absorption. The deduced effective recombination coefficient α shows the well-known decrease both with flare intensity and height, from 10^{-9} to 10^{-14} m^3/s (e.g. Hayes et al., 2017). The regression line deduced from all the presently evaluated 79 (h,α) points compares most favourably to

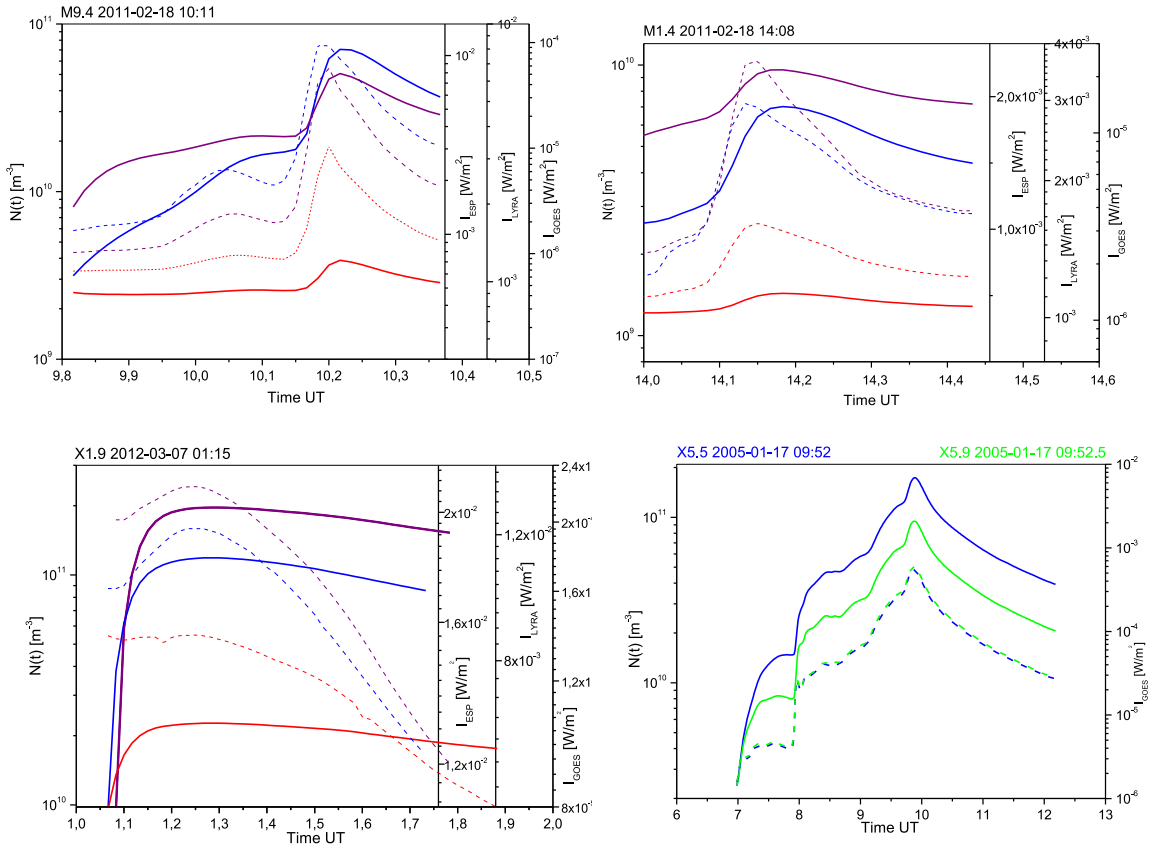

Fig. 12. Time evolution of the observed solar irradiance (dashed lines) and of the flare induced electron density at 90 km height (solid lines), as evaluated by the $N(t,h)$ model for the M9.4 and the M1.4 flares on 2011-02-18, the X1.9 flare on 2012-03-07, and the X5.5 and X5.9 flares on 2005-01-17. Irradiance observations by GOES15, ESP, and LYRA, and the corresponding electron densities are presented by blue, purple, and red lines respectively in the two top panels and the left bottom one. On the bottom right panel observations by GOES10 and GOES12, and the corresponding electron densities are presented by green and blue, respectively. (For interpretation of the references to colour in this figure legend, the reader is referred to the Web version of this article.)

Table 4
Measured and evaluated VLF *amplitude* time delay, for flares simultaneously observed by GOES, ESP and LYRA. Analogous VLF *phase* time delay* for the flares X5.5 (X5.9) observed by GOES only.

FLARE CLASS yyyy-mm-dd hh:mm UT	Instrument	Δt [min]	Δt_{ev} [min]
M9.4 2011-02-18 10:11	GOES15	2	1.94
	ESP	1	0.92
	LYRA	1	0.93
M1.4 2011-02-18 14:08	GOES15	3	2.82
	ESP	2	1.91
	LYRA	2	2.05
X1.9 2012-03-07 01:15	GOES15	2.5	2.49
	ESP	2.5	2.45
	LYRA	2.5	2.03
X5.9 2005-01-17 09:52.5	GOES10*	0.5	0.42
X5.5 2005-01-17 09:52	GOES12 *	1	0.95

Gledhill's (1986) recommended values, and the high-latitude α values of Friedrich et al. (2004) which result from rocket measured electron densities related to particle and X-ray fluxes. In particular the α values for the X5.9 flare (mid-latitude VLF data) are strongly comparable to those of Osepian et al. (2009), referring to the *same* event (2005-01-17 09:50–09:53 UT) though at high latitudes.

The contribution of different wavelength intervals to the ionization efficiency of the instruments' bandpass ranges being inspected, confirms that up to 90 km height the 0.1–0.8 nm band strongly dominates (consistent with other recent work, e.g., George et al. (2019)). The most effective ionization of the sub-nanometer wavelength interval occurs at around 90 km, producing a maximum in N (e.g. Richmond and Venkateswaran, 1971; Hargreaves 1992). The presented $N(t,h)$ model accounts for this property with the combined characteristics of LIE and SSI. With the increase of height both the LIE short-wavelength maximum is shifted to larger wavelengths and the declining LIE λ-gradient is notably reduced (LIE curves for 90–100 km, Fig. 6 inset). This makes LIE values at 90 km overwhelm the values at higher altitudes within the whole 0.1–0.8 nm range. With the increase of XPS SSI in this wavelength interval (Fig. 7), a maximum in ionization efficiency is produced, giving rise to analogous maxima in the ionization rate and the electron density. The result is that GOES data in the 0.1–0.8 nm band can be safely used to estimate the N increase during solar X-ray flares up to 90 km. Above 90 km wavelengths larger than 0.8 nm are responsible for ionization and the use of GOES irradiance only, leads to increasingly underestimated k and N values.

Up to 85 km the importance of the 1–2 nm band is minor: the respective contribution to k being 2 to 3 orders of magnitude below the one of the GOES bandpass, but increases notably with further increase of height, equaling the one of the 0.1–0.8 band at 95 km and surpassing it by an order of magnitude at 100 km. The 2–6 nm band behaves similarly: its almost negligible contribution to k up to 85 km rapidly increases above this height to equal in order of magnitude the one of the 1–2 band at 100 km. At above 90 km the important ionization band is 1–10 nm, still, within it, the 1–2 nm range contribution is dominant, due to the XPS SSI most prominent maximum in this domain (Fig. 7). The prediction of N, according to the 0.1–7 nm bandpass of ESP is likely to be reliable in the whole examined height range, showing reasonable agreement with the predictions of the GOES bandpass up to 90 km.

Very low values of N predicted by LYRA at 90 km, can be accounted for from the present analysis as due to three circumstances: XPS SSI is confirmed to be underestimated in the region 1–15 nm (Woods et al., 2008); the gap in the LYRA bandpass, excludes the 2–6 nm range, which becomes increasingly influential with height; the contribution to k from the band above 6 nm (the main LYRA bandpass) is negligible at the heights examined. Consequently, the ionization efficiency of the LYRA bandpass at 90 km builds up completely on the 1–2 nm band, which is insufficient in view of the increasing importance of the wavelengths above 2 nm at this height. (This effect is, clearly, all the more pronounced at heights below 90 km, producing inapplicably low LYRA k values.) Therefore, LYRA irradiance can provide estimates of N only above 90 km. These are lower than the estimates of N obtained with the ESP irradiance: by factors 2 and 1.5 for M1.4, by factors 3.6 and 2.9 for M9.4 and by factors 1.8 and 1.3 for X1.9, at 95 and 100 km respectively.

The present $N_{\max}(h)$ results are contrasted with the prediction of the standard LWPC simulation, which is known to be most reliable in the 60–90 km range, giving rather overestimated N values outside this domain. Despite this deficiency the comparison seems sensible enough, with improved mutual agreement for X-class flares, (Fig. 10 c and 11).

In particular we draw attention to the complex and highly dynamic event on 2005-01-17, within the sequence of very active days in January 2005, which include both flares and SPEs, though only GOES data are available for this event prior to the launching of SDO and PROBA2. The reason for this choice is that within the time interval (09:50–10:25 UT), comparison with other observations and models is provided, giving independent confirmation of the proposed method. The maximum in $N(09:53\ \mathrm{UT}, h)$ predicted by the $N(t,h)$ method at around 90 km is confirmed by the N measurements of the Tromsø EISCAT radar (224 MHz), at 09:53 UT, as well as by the modelled N values of Osepian et al. (2009) for the SPE at 09:50 UT (Fig. 11). Good agreement is found between the presently evaluated $N(10:25\ \mathrm{UT}, h)$for the X5.9 flare and N values deduced by Singer et al. (2011) from the Andenes radar measurements, in the height interval 56–67 km at 10:25 UT. The evaluated $N(t,h)$ and Tromsø radar N data (09:53 UT) converge towards higher altitudes, though the latter are lower by almost an order of magnitude at the lowest heights. These discrepancies can be, at least partly, attributed to the overestimation of the low wavelength domain brought about by the XPS SSI used in the present model.

As far as measurements are concerned, the $N(t,h)$ model relies on observed flare ISI and on VLF time delay (Δt_A or Δt_P). Physically, Δt it is the delay in the response of the ionosphere to enhanced (photo)ionization due to concurrent recombination processes. In a number of recent studies on ionospheric effects of solar flares by using VLF propagation (Hayes et al., 2017; George et al., 2019; Milligan et al., 2020; Belcher et al., 2021), the importance of time delay has been acknowledged and emphasized. When it comes to the Δt observable, only positive values are approved, ($\Delta t > 0$, as defined by Eq. (7)), since those bear the physical meaning of the 'sluggishness' in the ionospheric response (Appleton, 1953). The $N(t,h)$ method requires a *positive* time delay, either $\Delta t_A > 0$ or $\Delta t_P > 0$, as shown by the cases analyzed presently. However, for strong X-class flares, in particular for those associated with either CME and SPE, or more impulsive radiation, the perturbed VLF signal amplitude (e.g. Fig. 5, flare X5.5/X5.9) or *both* (A,P) (e.g. Fig. 4, flare X7.7) may peak before the flare, leading to $\Delta t < 0$.

We envisage that extreme X-ray flares, detected in the in 0.1–0.8 nm range, with 'negative' time delay of the VLF amplitude/phase with respect to the flare maximum, are to be considered within a wider picture of solar drivers, allowing for the flare specific spectral composition, as well as for other possible concurrent severe solar events. The resulting analysis makes apparent that $\Delta t < 0$ is an *indicator* that *other* drivers, closely preceding or coinciding with the flare, as detected in the 0.1–0.8 band, are present and that it is *them* that dominate the ionization, be it harder X-rays or CMEs or energetic particles bursts. This view is strongly supported by the recent works of Hayes et al. (2021) and Briand et al. (2022).

For the events studied here, the $N(t,h)$ model makes use of Δt_A, with the exception of the 2005-01-17 event, for which Δt_P is taken (Δt_A being negative). To the knowledge of the authors, Δt_P is here presented and used in evaluations for the first time. The electron density results for the X5.5(X5.9) flares, show both height and time profiles in remarkable agreement with independent observations and models. This demonstrates that Δt_P can be successfully deployed in the $N(t,h)$ model. One would go further and infer that in future studies, using the *pair* (Δt_A , Δt_P), for a particular flare, whenever feasible, will better determine the possible limits of the flare-induced electron density variation.

The extension of the $N(t,h)$ method to describe the combined effect of flares and SPE on the lower ionosphere is to be resolved, most likely by introducing to the continuity equation additional terms, e.g. the SPE ionization rate and reevaluating the ionization efficiency to include mechanisms of ionization other than photoionization. As VLF receivers monitor the actual response of the ionosphere with the complete coverage of the disturbed ionization state, regardless of the specific ionization agent in action, VLF observations will provide the *valid* time delay with respect to any, particular dominant solar driver present.

7. Conclusions

The work described in this paper studies how different spectral components of a solar flare influence the ionospheric response at different altitudes of the lower ionosphere. The presented $N(t,h)$ model solves the time-dependent continuity equation on a height span of 55–100 km, at the resolution of 5 km. X-ray and EUV irradiance measured during solar flares, by GOES(0.1–0.8 nm), ESP(0.1–7 nm) and LYRA(1–2 + 6–20 nm) and coincident ground measurements of (A,P) of the VLF signal propagating along the Earth-ionosphere waveguide are used to drive the model. Parallel inspection of these measurements brings forward a parameter correlating the two classes of observation – the time lag of the extreme VLF amplitude and/or phase behind the maximum flare irradiance - the *time delay*, (Δt_A and/or Δt_P), particular to each solar flare and VLF propagation path. It is the time delay that discerns the difference between electron density at *maximum flare irradiance* and the *maximum electron density* induced by the flare. This distinction leads to a salient feature of the proposed $N(t,h)$ model: the effective recombination coefficient needs not to be assumed, but is determined within the model itself.

The ionization efficiency $k(t_{I_{max}},h)$ and the ionization rate $q(t,h)$, throughout the flare duration, are evaluated for each particular flare as detected by the bandpass of the respective instrument, using the XPS model of the SSI (Woods et al., 2008) and the LIE data (Ohshio et al., 1966). Each flare is, therefore, treated as an individual event, determined not only by its flare class, but by its ionization efficiency (k) within *each spectral band* and by the response of the ionosphere through the related effective recombination coefficient (α).

Solving the time-dependent continuity equation for several M to X class flares, yields the development of the flare induced electron density from the beginning to the end of the flare event. It is found that the $N(t)$ curves follow most remarkably the behaviour of the respective flare irradiances as observed by GOES, ESP and LYRA (Fig. 12), distinctly displaying a time delay. The *evaluated* time delay deduced from the electron density time-profile is found to be in good agreement with the respective *measured* value, discrepancies amounting generally below 8% (Table 4). Thus, the *evaluated* time delay is one parameter which provides a criterion for the validity of the model.

Despite the drawbacks acknowledged, the electron densities and recombination coefficients, obtained with flare irradiances measured by GOES, ESP and LYRA compare favourably with independently modelled and observed values. The extent to which the ISI, as measured over the bandpass ranges of GOES, ESP and LYRA, is efficient in producing ionization changes, at heights of 55–100 km is accounted for. The results arrived at, suggest that the $N(t,h)$ method could be taken as a reliable first-order approximation in predicting the electron density time-height

profile for 55–100 km altitude, during X-ray solar flares, provided it is accompanied by careful spectral and temporal analysis of the flares studied.

Declaration of competing interest

The authors declare that they have no known competing financial interests or personal relationships that could have appeared to influence the work reported in this paper.

Data availability

Data will be made available on request.

Acknowledgements

This research was performed within the frame of the Guest Investigator Programme of the PROBA2 Science Center of the Royal Observatory of Belgium. V. Žigman acknowledges the guest investigator stay at ROB. We acknowledge the use of GOES (XRS) data from https://www.ngdc.noaa.gov/stp/satellite/goes/dataaccess.html, SDO(ESP) data from https://lasp.colorado.edu/home/eve/; PROBA2(LYRA) data from https://proba2.sidc.be; TIMED.SEE data from http://lasps.colorado.edu/see/. We thank J. Machol of the NOAA Center for Environmental Information regarding the use of GOES XRS data and in indicating the relevant NOAA data links. The assistance of I. Häggström in using the EISCAT Tromsø VHF radar data (https:/madrigal.eiscat.se/madrigal/) is gratefully acknowledged. EISCAT is an international association supported by research organisations in China (CRIRP), Finland (SA), Japan (NIPR and ISEE), Norway (NFR), Sweden (VR), and the United Kingdom (UKRI). The VLF data from the Belgrade VLF Observatory were retrieved through a collaborative project between the Institute of Physics, University of Belgrade, Serbia and the University of Nova Gorica, Slovenia. VLF data from Casey, Antarctica were obtained in collaboration with the VERSIM IAGA joint working group with support from the Australian Antarctic Division, and can be found at Data Coverage - Casey ULTRA by Variants (nerc-bas.ac.uk) We thank W. Singer for kindly providing the Singer et al. (2011) electron density data in tabular form. LYRA is a project of the Center Spatial de Liège, the Physikalisch-Meteorologisches Observatorium Davos and the Royal Observatory of Belgium, funded by the Belgian Federal Science Policy Office (BELSPO) and by the Swiss Bundesamt für Bildung und Wissenschaft. M. Dominique work is funded by the Belgian Federal Science Policy Office through the ESA-PRODEX programme, grant No. 4000134474. The authors thank the Reviewers for helpful comments on the paper.

References

Ajello, M., et al., 2021. First Fermi -LAT solar flare catalogue. Astrophys. J. Suppl. 252 (2) https://doi.org/10.3847/1538-4365/abd32e.

Allen, C.W., 1965. The interpretation of the XUV solar spectrum. Space Sci. Rev. 4, 91–122. https://doi.org/10.1007/BF00347155.

Ananthakrishnan, S., Abdu, M.A., Piazza, L.R., 1973. D-region recombination coefficients and the short wavelength X-ray flux during solar flare. Planet. Space Sci. 21, 367–375. https://doi.org/10.1016/0032-0633(73)90035-4.

Appleton, E.V., 1953. A note on sluggishness of ionosphere. J. Atmos. Terr. Phys. 3 (5), 282–284. https://doi.org/10.1016/0021-9169(53)90129-9.

Aschwanden, Markus J., Boerner, Paul, Ryan, Daniel, Caspi, Amir, McTiernan, James M., Warren, Harry P., 2015. Global energetics of solar flares: II. Thermal energies. Astrophys. J. 802 (1) https://doi.org/10.1088/0004-637X/802/1/53 article id. 53, 20.

Belcher, S.R.G., Clilverd, M.A., Rodger, C.J., Cook, S., Thomson, N.R., Brundell, J.B., Raita, T., 2021. Solar flare X-ray impacts on long subionospheric VLF paths. Space Weather 19, e2021SW002820. https://doi.org/10.1029/2021SW002820.

Benz, A.O., 2017. Flare observations, living. Rev. Solar Phys. 14 (1) https://doi.org/10.1007/s41116-016-0004-3 article id. 2.

Briand, C., Clilverd, M., Inturi, S., Cecconi, B., 2022. Role of hard X-ray emission in ionospheric D-layer disturbances during solar flares. Earth Planets Space 74, 41. https://doi.org/10.1186/s40623-022-01598-2.

Budden, K.G., 1988. The Propagation of Radio Waves: the Theory of Radio Waves of Low Power in the Ionosphere and Magnetosphere, first ed. Cambridge University Press. ISBN 0521369522.

Chamberlin, P., Woods, T., Eparvier, F., 2008. The flare irradiance spectral model (FISM) and its contributions to studies of the ionosphere and thermosphere. Space Weather 6 (5), S05001. https://doi.org/10.1029/2007SW000372.

Chamberlin, P.C., Eparvier, F.G., Knoer, V., Leise, H., Pankratz, A., Snow, M., Templeman, B., Thiemann, E.M.B., Woodraska, D.L., Woods, T.N., 2020. The flare irradiance spectral model-version 2 (FISM2). Space Weather 18 (12). https://doi.org/10.1029/2020SW002588.

Clilverd, M.A., Rodger, C.J., Thomson, N.R., Brundell, J.B., Ulich, T., Lichtenberger, J., Cobbett, N., Collier, A.B., Menk, F.W., Seppälä, A., Verronen, P.T., Turunen, E., 2009. Remote sensing space weather events: Antarctic–Arctic radiation-belt (dynamic) deposition-VLF atmospheric research Konsortium network. Space Weather 7, S04001. https://doi.org/10.1029/2008SW000412.

Collis, P.N., Hargreaves, J.K., White, G.P., 1996. A localised co-rotating auroral absorption event observed near noon using imaging riometer and EISCAT. Ann. Geophys. 14, 1305–1316. https://doi.org/10.1007/s00585-996-1305-y.

Cummer, S.A., 2000. Modeling electromagnetic propagation in the Earth-ionosphere waveguide. IEEE Trans. Antenn. Propag. 48 (9), 1420–1429. https://doi.org/10.1109/8.898776.

Dere, K.P., Landi, E., Mason, H.E., Monsignori Fossi, B.C., Young, P.R., 1997. CHIANTI - an Atomic Database for Emission Lines, vol. 125. A & A Supplement series, pp. 149–173. https://doi.org/10.1051/aas:1997368. October 1997.

Dolla, L., Marqué, C., Seaton, D.B., Van Doorsselaere, T., Dominique, M., Berghmans, D., Cabanas, C., De Groof, A., Schmutz, W., Verdini, A., West, M.J., Zender, J., Zhukov, A.N., 2012. Time delays in quasi-periodic pulsations observed during the X2.2 solar flare on 2011 february 15. Astrophys. J. Lett. 749 (1) https://doi.org/10.1088/2041-8205/749/1/L16 article id. L16.

Dominique, M., Hochedez, J.-F., Schmutz, W., Dammasch, I.E., Shapiro, A.I., Kretzschmar, M., Zhukov, A.N., Gillotay, D., Stockman, Y., BenMoussa, A., 2013. The LYRA instrument onboard PROBA2: description and in-flight performance. Sol. Phys. 286 (1), 21–42. https://doi.org/10.1007/s11207-013-0252-5.

Enell, Carl-Fredrik, Jonas, Hedin, Jacek Stegman, Witt, Georg, Friedrich, Martin, Singer, Werner, Baumgarten, Gerd, Kaifler, Bernd, Hoppe, Ulf-Peter, Gustavsson, Björn, Khaplanov, Mikhail, Kero, Antti, Ulich, Thomas, Turunen, Esa, Urban Brändström, 2011. The Hotel Payload 2 campaign: overview of NO, O and electron density measurements in the upper mesosphere and lower thermosphere. J. Atmos. Sol. Terr. Phys. 73 (14–15), 2228–2236. https://doi.org/10.1016/j.jastp.2011.01.001. ISSN 1364-6826.

Ferguson, J.A., 1998. Computer Programs for Assessment of Long-Wavelength Radio Communications, Version 2.0: User's guide and source files. SPAWAR Technical Document 3030. Space and Naval Warfare Systems Center, San Diego, California. https://apps.dtic.mil/sti/pdfs/ADA350375.pdf.

Ferguson, J.A., Snyder, F.P., 1990. Computer Programs for Assessment of Long Wavelength Radio Communications, Tech. Doc. 1773, Natl. Ocean Syst. Cent., San Diego, California.

Friedrich, M., Torkar, K.M., Steiner, R.J., 2004. Empirical recombination rates in the lower ionosphere. Adv. Space Res. 34, 1937–1942. https://doi.org/10.1016/j.asr.2004.04.010.

George, H.E., Rodger, C.J., Clilverd, M.A., Cresswell-Moorcock, K., Brundell, J.B., Thomson, N.R., 2019. Developing a nowcasting capability for X-class solar flares using VLF radiowave propagation changes. Space Weather 17, 1783–1799. https://doi.org/10.1029/2019SW002297.

Gledhill, J.A., 1986. The effective recombination coefficient of electrons in the ionosphere between 50 and 150 km. Radio Sci. 21 (3), 399–407. https://doi.org/10.1029/RS021i003p00399.

Gross, N.C., Cohen, M.B., Said, R.K., Golkowski, M., 2018. Polarization of narrowband VLF transmitter signals as an ionospheric diagnostic. J. Geophys. Research: Space Phys. 123, 901–917. https://doi.org/10.1002/2017JA024907.

Grubor, D.P., Šulić, D.M., Žigman, V., 2008. Classification of X-ray solar flares regarding their effects on the lower ionosphere electron density profile. Ann. Geophys. 26, 1731–1740. https://doi.org/10.5194/angeo-26-1731-2008.

Häggström, I., 2005. Data from the CEDAR Madrigal Database. EISCAT Scientific Association. https://w3id.org/cedar?experiment_list=experiments/2005/eis/01jul05&file_list=MAD6300_2005-07-01_arcd_60@vhf.hdf5 (Accessed 23 May 2022).

Hargreaves, J.K., 1992. The Solar-Terrestrial Environment, first ed. Cambridge University Press, Cambridge, 0521327482.

Hargreaves, J.K., 2005. A new method of studying the relation between ionization rates and radio-wave absorption in polar-cap absorption events. Ann. Geophys. 23, 359–369. https://doi.org/10.5194/angeo-23-359-2005.

Hargreaves, J.K., Birch, M.J., 2018. Observations by incoherent scatter radar of related D- and F-region structuring at very high latitude. J. Atmos. Sol. Terr. Phys. 174, 5–16. https://doi.org/10.1016/j.jastp.2018.01.032.

Hayes, L.A., Gallagher, P.T., McCauley, J., Dennis, B.R., Ireland, J., Inglis, A., 2017. Pulsations in the Earth's lower ionosphere synchronized with solar flare emission. J. Geophys. Res. Space Phys. 122, 9841–9847. https://doi.org/10.1002/2017JA024647.

Hayes, L.A., O'Hara, O.S.D., Murray, S.A., Gallagher, P.T., 2021. Solar flare effects on the Earth's lower ionosphere. Sol. Phys. 296, 157. https://doi.org/10.1007/s11207-021-01898-y.

Landi, E., Del Zanna, G., Young, P.R., Dere, K.P., Mason, H.E., 2012. CHIANTI—an atomic database for emission lines. XII. Version 7 of the database. Astrophys. J. 744 (2) https://doi.org/10.1088/0004-637X/744/2/99 article id. 99, 9 pp.

Machol, J., Viereck, R., Peck, C., Mothersbaugh III, J., 2022. GOES X-ray sensor (XRS) operational data. https://ngdc.noaa.gov/stp/satellite/goes/doc/GOES_XRS_readme.pdf. (Accessed 6 April 2023) accessed.

McRae, M.W., Thomson, N.R., 2000. VLF phase and amplitude: daytime ionospheric parameters. J. Atmos. Sol. Terr. Phys. 62, 609–618. https://doi.org/10.1016/S1364-6826(00)00027-4.

McRae, W.M., Thomson, N.R., 2004. Solar flare induced ionospheric D-region enhancements from VLF amplitude observations. J. Atmos. Sol. Terr. Phys. 66, 77–87. https://doi.org/10.1016/j.jastp.2003.09.009.

Milligan, R.O., Hudson, H.S., Chamberlin, P.C., Hannah, I.G., Hayes, L.A., 2020. Lyman-Alpha Variability during Solar Flares over Solar Cycle 24 Using GOES-15/EUVS-E, vol. 18. Space Weather, e2019SW002331.

Mitra, A., 1974. Ionospheric Effects of Solar Flares, first ed. D. Reidel Publishing Company, Dordrecht,Holland. ISBN 90277467.

NOAA SESC: solar proton events affecting the Earth Environment. https://umbra.nascom.nasa.gov/SEP/, 2023–. (Accessed 16 February 2023) accessed.

NOAA SWPC: solar proton events affecting the Earth environment. ftp://ftp.swpc.noaa.gov/pub/indices/SPE.txt, 2020–. (Accessed 22 January 2020) accessed.

Ohshio, M., Maeda, R., Sakagami, H., 1966. Height distribution of local ionization efficiency. J. Radio Res. Lab. 13 (70), 245–261. https://www.nict.go.jp/publication/journal/13/070/Journal_Vol13_No070_index.pdf. (Accessed 27 May 2022). accessed.

Osepian, A., Kirkwood, S., Dalin, P., Tereschenko, V., 2009. D-region electron density and effective recombination coefficients during twilight– experimental data and modelling during solar proton events. Ann. Geophys. 27, 3713–3724. https://doi.org/10.5194/angeo-27-3713-2009.

Pappert, R.A., Snyder, F.P., 1972. Some results of a mode-conversion program for VLF. Radio Sci. 7, 913. https://doi.org/10.1029/RS007i010p00913.

Ratcliffe, J.A., 1972. An Introduction to the Ionosphere and Magnetosphere, first ed. Cambridge University Press, Cambridge. ISBN 0521083419.

Richmond, A.D., Venkateswaran, S.V., 1971. Geomagnetic crochets and associated ionospheric current systems. Radio Sci. 6, 139–164. https://doi.org/10.1029/RS006i002p00139.

Rishbeth, H., Garriott, O.K., 1969. Introduction to Ionospheric Physics, first ed. Academic Press, New York, London.

Rodger, C.J., Molchanov, O.A., Thomson, N.R., 1998. Relaxation of transient ionization in the lower ionosphere. J. Geophys. Res. 103 (A4), 6969–6975. https://doi.org/10.1029/98JA00016.

Singer, W., 2012. Private Communication.

Singer, W., Latteck, R., Friedrich, M., Wakabayashi, M., Rapp, M., 2011. Seasonal and solar activity variability of D-region electron density at 69^{o} N. J. Atmos. Sol. Terr. Phys. https://doi.org/10.1016/j.jastp.2010.09.012.

Thomson, N.R., 1993. Experimental daytime VLF ionospheric parameters. J. Atmos. Sol. Terr. Phys. 55 (2), 173–184.

Thomson, N.R., Clilverd, A.M., 2000. Solar cycle changes in daytime VLF subionospheric attenuation. J. Atmos. Sol. Terr. Phys. 62, 601–608. https://doi.org/10.1016/0021-9169(93)90122-F.

Thomson, N.R., Clilverd, M.A., 2001. Solar flare induced ionospheric D-region enhancements from VLF amplitude observations. J. Atmos. Sol. Terr. Phys. 63, 1729–1737. https://doi.org/10.1016/S1364-6826(01)00048-7.

Thomson, N.R., Rodger, C.J., Dowden, R.L., 2004. Ionosphere gives size of greatest solar flares. Geophys. Res. Lett. 31, L06803 https://doi.org/10.1029/2003GL019345.

Thomson, N.R., Rodger, C.J., Clilverd, M.A., 2005. Large solar flares and their ionospheric D region enhancements. J. Geophys. Res. 110, A06306 https://doi.org/10.1029/2005JA011008.

Thomson, N.R., Clilverd, M.A., Rodger, C.J., 2011. Daytime mid-latitude D-region parameters at solar minimum from short path VLF phase and amplitude. J. Geophys. Res. 116, A03310 https://doi.org/10.1029/2010JA016248.

Thomson, N.R., Clilverd, M.A., Rodger, C.J., 2017. Midlatitude ionospheric D region: height, sharpness and solar zenith angle. J. Geophys. Res. 122, 8933–8946. https://doi.org/10.1002/2017JA024455.

Thomson, N.R., Clilverd, M.A., Rodger, C.J., 2022. Ionospheric *D* region: VLF-measured electron densities compared with rocket-based FIRI-2018 model. J. Geophys. Res.: Space Phys. 127, e2022JA030977 https://doi.org/10.1029/2022JA030977.

Wait, J.R., Spies, K.P., 1964. NBS Technical Note 300 Characteristics of the Earth-Ionosphere Waveguide for VLF Radio Waves. National Bureau of Standards.

Wenzel, D., Jakowski, N., Berdermann, J., Mayer, C., Valladares, C., Heber, B., 2016. Global ionospheric flare detection system (GIFDS). J. Atmos. Sol. Terr. Phys. 138, 233–242. https://doi.org/10.1016/j.jastp.2015.12.011.

Whitten, R.C., Poppoff, I.G., 1965. Physics of the Lower Ionosphere. Prentice-Hall, Englewood Cliffs, NJ.

Woods, Thomas N., Chamberlin, Phillip C., Peterson, W.K., Meier, R.R., Richards, Phil G., Strickland, Douglas J., Lu, Gang, Qian, Liying, Solomon, Stanley C., Iijima, B.A., Mannucci, A.J., Tsurutani, B.T., 2008. XUV photometer system (XPS): improved solar irradiance algorithm using CHIANTI spectral models. Sol. Phys. 250 (2), 235–267. https://doi.org/10.1007/s11207-008-9196-6.

Woods, T.N., Eparvier, F.G., Hock, R., Jones, A.R., Woodraska, D., Judge, D., Didkovsky, L., Lean, J., Mariska, J., Warren, H., McMullin, D., Chamberlin, P., Berthiaume, G., Bailey, S., Fuller-Rowell, T., Sojka, J., Tobiska, W.K., Viereck, R., 2012. Extreme ultraviolet variability experiment (EVE) on the solar dynamics observatory (SDO): overview of science objectives, instrument design, data products, and model developments. Sol. Phys. 275 (1–2), 115–143. https://doi.org/10.1007/s11207-009-9487-6.

Xu, W., Marshall, R.A., Bortnik, J., Bonnell, J.W., 2021. An electron density model of the D- and E-region ionosphere for transionospheric VLF propagation. J. Geophys. Res.: Space Phys. 126 (7), e2021JA029288 https://doi.org/10.1029/2021JA029288.

Žigman, V., Grubor, D., Šulić, D., 2007. D-region electron density evaluated from VLF amplitude time delay during X-ray solar flares. J. Atmos. Sol. Terr. Phys. 69, 775–792. https://doi.org/10.1016/j.jastp.2007.01.012.

Žigman, V., Kudela, K., Grubor, D., 2014. Response of the Earth's lower ionosphere to the ground level enhancement event of december 13, 2006. Adv. Space Res. 53, 763–775. https://doi.org/10.1016/j.asr.2013.12.026.